Theoretical description of semi-inclusive T2K, MINERνA and MicroBooNE neutrino-nucleus data in the relativistic plane wave impulse approximation

J. M. Franco-Patino,[1,2] M. B. Barbaro,[2,3] J. A. Caballero,[1,4] and G. D. Megias[5,1]

[1]*Departamento de Física atómica, molecular y nuclear, Universidad de Sevilla, 41080 Sevilla, Spain*
[2]*Dipartimento di Fisica, Università di Torino and INFN, Sezione di Torino,*
Via P. Giuria 1, 10125 Torino, Italy
[3]*Université Paris-Saclay, CNRS/IN2P3, IJCLab, 91405 Orsay, France*
[4]*Instituto de Física Teórica y Computacional Carlos I, Granada 18071, Spain*
[5]*Research Center for Cosmic Neutrinos, Institute for Cosmic Ray Research, University of Tokyo,*
Kashiwa, Chiba 277-8582, Japan

We present the results of semi-inclusive neutrino-nucleus cross sections within the plane wave impulse approximation (PWIA) for three nuclear models: relativistic Fermi gas, independent-particle shell model, and natural orbital shell model in comparison with the available CC0π measurements from the T2K, MINERνA, and MicroBooNE collaborations where a muon and at least one proton are detected in the final state. Results are presented as a function of the momenta and angles of the final particles, as well as in terms of the imbalances between proton and muon kinematics. The present semi-inclusive formalism is based on fully relativistic microscopic calculations and numerical integrations to produce both lepton and hadron kinematics without relying on further approximations. The analysis reveals that contributions beyond PWIA are crucial to explain the experimental measurements and that the study of correlations between final-state proton and muon kinematics can provide valuable information on relevant nuclear effects such as the Fermi motion and final-state interactions.

I. INTRODUCTION

The study of neutrino oscillation is a valuable tool that can be used for extracting neutrino mixing angles, mass-squared differences, and the *CP*-symmetry violation phase as well as for looking for hints of new physics beyond the standard model in the electroweak sector [1,2].

The oscillation probability is a function of the neutrino propagation distance and of its energy. In accelerator-based oscillation experiments, the neutrino propagation distance is well known. However, as these experiments do not use monochromatic neutrino beams, the accuracy to which they can extract neutrino oscillation parameters depends on their ability to determine the energy of the incoming neutrinos. This relies on a proper understanding of the scattering of neutrinos with nucleons in the target and of the nuclear-medium effects involved, which are among the most relevant limiting factors for oscillation measurements [2–6]. Experimentally, the energy of incoming neutrinos is reconstructed from the particles generated after their interaction with the nuclear target. Therefore, to reduce the associated systematic uncertainties, it is essential to be able to precisely model neutrino interactions with nuclei, such as ^{12}C, ^{16}O, or ^{40}Ar, that are commonly used as targets. In some neutrino experiments, such as T2K or MicroBooNE, the events detected at relevant energies are dominated by charged-current (CC) neutrino-nucleon quasielastic (QE) scattering interactions, where the neutrino removes a single nucleon from the nucleus without producing any additional particles. These reactions can be reasonably well approximated as two-body interactions, and their experimental signature of an identifiable lepton is relatively straightforward to measure. However, other non-QE processes such as multinucleon excitations—mainly the excitation of two-particle/two-hole (2p2h) states—of the nucleus, where a charged lepton and two nucleons are emitted, can mimic a charged-current quasielastic (CCQE) event in the detectors, thus affecting the reconstruction of the neutrino energy which assumes CCQE. As a result, the CCQE reaction is not directly accessible, and what is experimentally measured are the so-called CC0π events, i.e., CC interactions with a charged lepton and no pions detected in the final state. Multinucleon excitations together with initial-state nucleon-nucleon (NN) correlations and other effects related to the propagation of the knockout nucleons through the nuclear medium must be included in the data analysis. The distributions of final-state lepton kinematics have been widely measured for the CC0π topology [7–16], yet an accurate identification of the reaction

073008-1

channels related to the different nuclear processes described above has been found difficult. This is because the lepton final-state kinematics is largely affected by the nuclear dynamics.

In this context, one way to significantly improve the reconstruction of the neutrino energy together with the experimental systematic uncertainties is the analysis of more exclusive processes where selection criteria are also placed on the particle content of the hadronic system; i.e., in addition to the final lepton as in purely inclusive measurements, other particles are also detected. For example, this is the case of semi-inclusive events in which the lepton is detected in coincidence with one hadron in the final state. Accordingly, the T2K, MINERvA, and MicroBooNE collaborations are each performing measurements of topologies involving one charged lepton detected in coincidence with one or more particles in the final state [17–21]. Also, forthcoming projects and experiments such as SK-Gd [22], HyperKamiokande [23], and DUNE [24] are making important efforts to improve the detection and identification capabilities of final-state hadrons. Thus, it is crucial to have realistic theoretical nuclear models for the description of semi-inclusive processes, whose formalism is more complex but that make possible to analyze nuclear effects not accessible with inclusive processes that are relatively insensitive to the details of the final nuclear states.

In Ref. [25], we presented a study of semi-inclusive CC neutrino-nucleus reactions in the plane wave impulse approximation (PWIA) for several nuclear models. In this work, we apply this analysis to compare our predictions with the available semi-inclusive experimental data where a muon and at least one proton are detected in the final state. Results are compared with recent data from the T2K [17], MINERvA [18,19] (ν_μ on ^{12}C), and MicroBooNE [20,21] (ν_μ on ^{40}Ar) collaborations. Although being aware of the oversimplified description of the reaction provided by PWIA, the present study is meant to be a first step toward a more complete modeling and a useful benchmark for more sophisticated calculations. Not only does the

comparison with these data illustrate our methods, but it also allows us to identify the kinematics where effects beyond PWIA are expected to play an important role.

This paper is organized as follows. In Sec. II, we present a summary of the general semi-inclusive neutrino-nucleus scattering formalism in the PWIA and provide analytic expressions of the flux-integrated fifth-differential semi-inclusive neutrino-nucleus cross sections for three different nuclear models: relativistic Fermi gas (Sec. II A), independent-particle shell model (Sec. II B), and natural orbitals shell model (Sec. II C). Given that neutrino collaborations have presented the semi-inclusive experimental data as function of different variables, in Sec. III, we define the three sets of observables employed in experimental analyses and give their expressions as function of the momentum and angles of the particles detected in the final state, i.e., a muon and a proton in all cases considered in this work. Next, we present the comparison of our theoretical results with the available semi-inclusive data from T2K (Sec. IV A), MINERvA (Sec. IV B), and MicroBooNE (Sec. IV C). Finally, in Sec. V, we summarize our conclusions.

II. SEMI-INCLUSIVE NEUTRINO-NUCLEUS REACTIONS FORMALISM

Following the theoretical work started in Refs. [26] and [27], we studied in Ref. [25] the semi-inclusive neutrino-nucleus cross sections in the PWIA for three different nuclear models: the relativistic Fermi gas (RFG) model, the independent-particle shell model (IPSM), and the energy-dependent natural orbit (NO) model for ^{12}C and ^{40}Ar. Here, we briefly summarize the main results of Ref. [25].

Assuming that a neutrino of momentum $\mathbf{k}$ interacts with an off-shell bound nucleon of momentum $\mathbf{p_m}$ exchanging a charged boson W, and a lepton of momentum $\mathbf{k}'$ is detected in coincidence with an ejected nucleon of momentum $\mathbf{p_N}$ in the final state, the semi-inclusive cross section of the process in the factorization approximation is given by

$$\frac{d\sigma}{dk'd\Omega_{k'}dp_Nd\Omega_N^L} = \frac{(G_F\cos\theta_c k'p_N)^2 m_N}{8k\varepsilon'E_N(2\pi)^6}\int_0^\infty d\mathcal{E}\int d^3p_m v_0\mathcal{F}_\chi^2 S(p_m,E_m)$$
$$\times\delta\left(M_A+\omega-E_N-\sqrt{p_m^2+M_{A-1}^2}-\mathcal{E}\right)\delta(\mathbf{q}-\mathbf{p_N}+\mathbf{p_m}),\quad(1)$$

where G_F is the Fermi constant; θ_c is the Cabibbo angle; $(\varepsilon', \Omega_{k'})$ and (E_N, Ω_N^L) are the energies and scattering angles of the final lepton and nucleon, respectively; $\omega = k - \varepsilon'$ is the transferred energy; and $\mathbf{q} = \mathbf{k} - \mathbf{k}'$ is the transferred momentum. $S(p_m, E_m)$ is the nuclear spectral function that describes the probability of finding a nucleon in a nucleus A with given momentum (called the missing momentum p_m) and with a given excitation energy

of the residual nuclear system $A - 1$ (called the missing energy E_m). The kinematic factor v_0 and the reduced single nucleon cross section $\mathcal{F}_\chi^2$ are defined in Appendix A of Ref. [25], and $\mathcal{E}$ is the difference in recoil energies between the residual nucleus with invariant mass W_{A-1} and one with minimum invariant mass M_{A-1}. Note that Eq. (1) depends on the neutrino momentum k, the final lepton variables (k', θ_l, ϕ_l), and also the final nucleon variables

$(p_N, \theta_N^L, \phi_N^L)$. For convenience, the neutrino direction is chosen as the z axis; therefore, θ_N^L is the angle between the final nucleon and the incoming neutrino, and ϕ_N^L is the angle between the scattering plane (defined by $\mathbf{k}$ and $\mathbf{k}'$) and the reaction plane (defined by $\mathbf{k}$ and $\mathbf{p_N}$). The two δ functions that appear in Eq. (1) guarantee the conservation of energy and momentum in the process.

In what follows, we briefly summarize the three different nuclear models considered in this work, namely, the RFG, IPSM, and NO, and obtain the analytical expressions for the semi-inclusive neutrino-nucleus cross section in each model, providing the explicit form of the spectral function $S(p_m, E_m)$. The normalization of the spectral function is chosen to be

$$\mathcal{N} = \frac{1}{(2\pi)^3} \int_0^\infty dp_m p_m^2 \int_0^\infty dE_m S(p_m, E_m) \qquad (2)$$

with $\mathcal{N}$ the number of nucleons that are active in the scattering, i.e., the number of neutrons for the case of neutrino scattering (CC_ν) and the number of protons for antineutrinos ($CC_{\bar\nu}$).

A. Relativistic Fermi gas

In the Relativistic Fermi gas model the nucleus is described as an infinite gas of free relativistic nucleons that, in the nuclear ground state, occupy all the levels up to the Fermi momentum k_F while the levels above that are empty. The Fermi momentum is the only free parameter of the model. It is usually fitted to the width of the quasielastic peak in electron scattering data and varies with the nucleus. As proposed in Ref. [27], we consider a shift in the RFG energies by a constant quantity in such a way that the last occupied level in the Fermi sea coincides with the separation energy $-E_s$, defined as the minimum energy necessary to remove a nucleon from the nucleus. This introduces a second parameter in the model, E_s, fitted to the position of the quasielastic peak. By doing this, the nucleons in the RFG model are no longer on shell because their free energy is changed as

$$E = \sqrt{p_m^2 + m_N^2} \to E - (E_F + E_s) \qquad (3)$$

with $E_F = \sqrt{k_F^2 + m_N^2}$ the Fermi energy. For this model, the normalized spectral function is [27]

$$S_{\text{RFG}}(p_m, \mathcal{E}) = \frac{3(2\pi)^3 \mathcal{N}}{k_F^3} \Theta(k_F - p_m)\delta(\mathcal{E} - E_F + E), \qquad (4)$$

where the Pauli principle is explicitly imposed by the Θ function and the energy conservation is imposed by the δ function.

Given a normalized neutrino flux $P(k)$, with k representing the neutrino momentum, the flux-averaged semi-inclusive neutrino-nucleus cross section for the RFG model is

$$\left\langle \frac{d\sigma}{dk' d\Omega_{k'} dp_N d\Omega_N^L} \right\rangle$$
$$= \frac{3\mathcal{N}(G_F \cos\theta_c m_N k' p_N)^2}{8(2\pi k_F)^3 \varepsilon' E_N}$$
$$\times \frac{P(k_0)}{k_0} \frac{v_0 \mathcal{F}_\chi^2}{E_B - p_B \cos\theta_B} \Theta(k_F - p_m)\Theta(p_N - k_F) \qquad (5)$$

with the neutrino momentum k_0 fixed by energy conservation to

$$k = k_0 = \frac{E_B^2 - p_B^2 - m_N^2}{2(E_B - p_B \cos\theta_B)} \qquad (6)$$

and where we have defined the following auxiliary variables:

$$\mathbf{p}_B = \mathbf{k}' + \mathbf{p}_N, \qquad (7)$$

$$E_B = \varepsilon' + E_s + E_F + E_N - m_N, \qquad (8)$$

$$p_B \cos\theta_B = k' \cos\theta_l + p_N \cos\theta_N^L. \qquad (9)$$

From momentum conservation, the missing momentum p_m is given by

$$p_m^2 = k_0^2 - 2k' k_0 \cos\theta_l + k'^2 + p_N^2 - 2k_0 p_N \cos\theta_N^L + 2k' p_N (\cos\theta_l \cos\theta_N^L + \sin\theta_l \sin\theta_N^L \cos\phi_N^L). \qquad (10)$$

Note that both k_0 and p_m are completely determined by the final-state kinematics.

B. Independent-particle shell model

In the IPSM, the bound nucleons are described by wave functions that are solutions of the Dirac-Hartree equation with real scalar and vector potentials and occupy discrete energy levels $-E_{nlj}$. The spectral function of this model is [27]

$$S_{\text{IPSM}}(p_m, \mathcal{E}) = \sum_{n,l,j}(2j + 1)n_{nlj}(p_m)\delta(\mathcal{E} + E_s - E_{nlj}), \qquad (11)$$

where $n_{nlj}(p_m)$ is the momentum distribution of a single nucleon in a shell characterized by the quantum numbers nlj. The flux-averaged semi-inclusive neutrino-nucleus cross section for this model is then

$$\left\langle \frac{d\sigma}{dk' d\Omega_{k'} dp_N d\Omega_N^L} \right\rangle = \frac{(G_F \cos\theta_c k' p_N)^2 m_N}{8(2\pi)^6 \varepsilon' E_N} \sum_{n,l,j} (2j+1)$$

$$\times \frac{P(k_{0nlj})}{k_{0nlj}} v_0 \mathcal{F}_\chi^2 n_{nlj}(p_m) \qquad (12)$$

with the neutrino momentum

$$k_{0nlj} = \varepsilon' + E_N - m_N + E_{nlj} \qquad (13)$$

and the missing momentum

$$p_m^2 = k_{0nlj}^2 + k'^2 + p_N^2 - 2k_{0nlj}k' \cos\theta_l - 2k_{0nlj}p_N \cos\theta_N^L$$
$$+ 2k' p_N (\cos\theta_l \cos\theta_N^L + \sin\theta_l \sin\theta_N^L \cos\phi_N^L) \qquad (14)$$

fixed by the energy and momentum conservation. Notice that, unlike the RFG case, for the IPSM, the final-state kinematics does not correspond to a definite neutrino energy. This is a consequence of the shell structure of the spectral function.

C. Natural orbitals shell model

This model is similar to the IPSM, but it takes into account NN correlations, defining the effects beyond the mean field due to the very strong interaction between the nucleons inside the nucleus that occur at short distances, and the smearing of the energy eigenstates. It employs natural orbitals, $\psi_i(r)$, defined as the complete orthonormal set of single-particle wave functions that diagonalize the one-body density matrix [28]:

$$\rho(\mathbf{r}, \mathbf{r}') = \sum_i N_i \psi_i^*(\mathbf{r}) \psi_i(\mathbf{r}'), \qquad (15)$$

where the eigenvalues $N_i (0 \leq N_i \leq 1, \sum_i N_i = A)$ are the natural occupation numbers and A is the mass number.

The NO single-particle wave functions are used to obtain the occupation numbers and the wave functions in momentum space, i.e., the momentum distributions, and from them the spectral function that is given by [29]

$$S_{NO}(p_m, \mathcal{E}) = \frac{1}{2\pi A} \sum_i (2j_i + 1) N_i |\psi_i(p_m)|^2 L_{\Gamma_i}(\mathcal{E} - \mathcal{E}_i), \qquad (16)$$

where the dependence upon the energy is given by the Lorentzian function

$$L_{\Gamma_i}(\mathcal{E} - \mathcal{E}_i) = \frac{1}{2\pi} \frac{\Gamma_i}{(\mathcal{E} - \mathcal{E}_i)^2 + (\Gamma_i/2)^2} \qquad (17)$$

with Γ_i the width for a given single-particle state and $\mathcal{E}_i$ the energy eigenvalue of the state.

The flux-averaged semi-inclusive neutrino-nucleus cross section in this model is given by

$$\left\langle \frac{d\sigma}{dk' d\Omega_{k'} dp_N d\Omega_N^L} \right\rangle$$
$$= \int d\mathcal{E} \frac{(G_F \cos\theta_c k' p_N)^2 m_N P(k)}{8k\varepsilon' E_N (2\pi)^7 A}$$
$$\times \sum_i (2j_i + 1) N_i |\psi_i(p_m)|^2 L_{\Gamma_i}(\mathcal{E} - \mathcal{E}_i) v_0 \mathcal{F}_\chi^2, \qquad (18)$$

where the neutrino momentum, for a given excitation energy $\mathcal{E}$, is

$$k = E_s + E_N + \varepsilon' - m_N + \mathcal{E} \qquad (19)$$

and

$$p_m^2 = k^2 + k'^2 + p_N^2 - 2kk' \cos\theta_l - 2kp_N \cos\theta_N^L$$
$$+ 2k' p_N (\cos\theta_l \cos\theta_N^L + \sin\theta_l \sin\theta_N^L \cos\phi_N^L). \qquad (20)$$

Note that in this case the integral over $\mathcal{E}$ in Eq. (18) has to be performed numerically because, unlike the IPSM, the single-particle energies are not discrete.

Momentum distributions for the three nuclear models considered are shown in Fig. 1 (bottom) for ^{12}C. In the case of ^{40}Ar, only two nuclear models are considered, namely, RFG and IPSM, because NO wave functions for ^{40}Ar are not available yet. The respective ^{40}Ar momentum distributions for the two nuclear models are also shown in Fig. 1 (top). Notice the difference between the IPSM and NO predictions for ^{12}C in the region of low missing momentum.

III. EXPERIMENTAL OBSERVABLES

The main objective of this work is to compare all the available semi-inclusive experimental data for different experiments, namely, T2K, MINERνA, and MicroBooNE, with theoretical predictions in the PWIA using different nuclear models. The kinematics of the outgoing muon and proton for semi-inclusive CC0π events is completely characterized by the independent variables $(k', \theta_l, p_N, \theta_N^L, \phi_N^L)$, which will be called natural variables (NV). In addition to these variables, we also introduce two more sets of variables used in the experimental analyses: the transverse kinematic imbalances (TKI) [19,30,31] and the inferred variables (IV) [17], which will be defined in the following sections.

A. Natural variables

The first and more straightforward way to characterize the final state is using the so-called natural variables defined in Fig. 2. Taking the z axis as the incoming neutrino direction, the final lepton momentum ($\mathbf{k}'$) forms an angle θ_l with the initial neutrino direction ($\mathbf{k}$), and the two vectors define the scattering plane (xz plane). After the
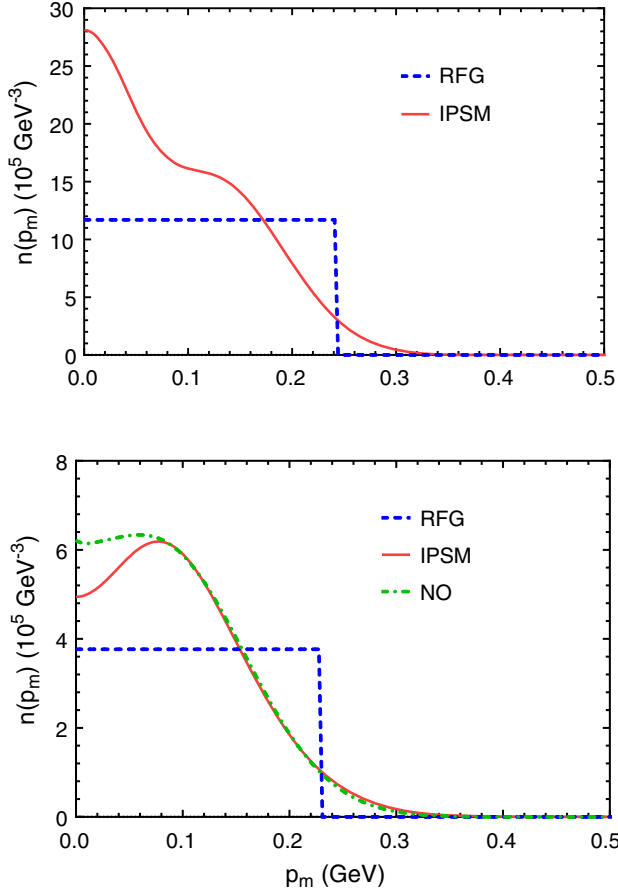
FIG. 1.   Momentum distributions for ^{40}Ar (top) and ^{12}C (bottom) normalized according to Eq. (2) for the three different nuclear models considered in this work, namely, RFG (blue dashed), IPSM (red solid), and NO (green dot-dashed).
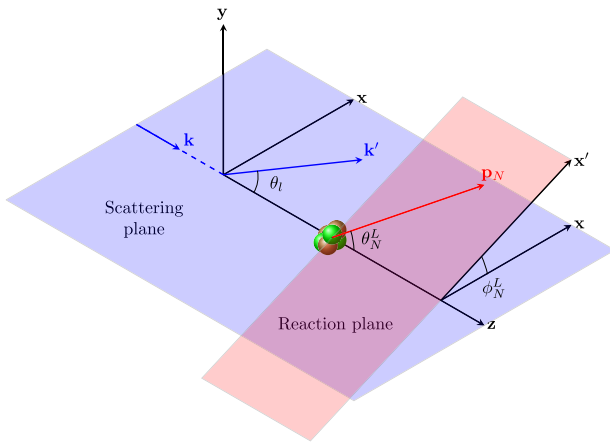

FIG. 2.   Schematic representation of the definition of the natural variables: k', θ_l, p_N, θ_N^L, and ϕ_N^L. The incoming neutrino ($\mathbf{k}$) and the final lepton ($\mathbf{k'}$) are contained in the scattering plane, while the reaction plane contains the incoming neutrino and the ejected nucleon.

interaction with the nucleus, a nucleon is ejected with momentum $\mathbf{p_N}$ forming an angle θ_N^L with the initial neutrino direction. The final nucleon is contained in a plane called the reaction plane ($x'z$ plane), which is rotated by an angle ϕ_N^L with respect to the scattering plane.

This set of variables will be used in the results section to analyze both semi-inclusive and inclusive CC0π; the latter are obtained by integrating Eq. (1) over the final nucleon variables.

The 3-momenta defined in the frame shown in Fig. 2 are

$$\mathbf{k} = k\mathbf{e}_z,$$

$$\mathbf{k'} = k'(\sin\theta_l\mathbf{e}_x + \cos\theta_l\mathbf{e}_z),$$

$$\mathbf{p}_N = p_N(\sin\theta_N^L\cos\phi_N^L\mathbf{e}_x + \sin\theta_N^L\sin\phi_N^L\mathbf{e}_y + \cos\theta_N^L\mathbf{e}_z).$$

$$(21)$$

B. Transverse kinematic imbalances

The TKI [30] are designed to enhance experimental sensitivity to nuclear effects, and therefore discriminate between different models, with minimal dependence on the neutrino energy. In particular, the use of TKI can help in disentangling effects linked to final-state interactions (FSIs), initial-state correlations, and/or multinucleon excitations (2p2h). They are defined by projecting the final lepton and the ejected nucleon momenta on the plane perpendicular to the neutrino direction (transverse plane) as can be seen in Fig. 3.

More specifically, the vector magnitude of the momentum imbalance (δp_T) and the two angles ($\delta\alpha_T$ and $\delta\phi_T$) are

$$\delta p_T = |\mathbf{k}'_T + \mathbf{p}_T^N|,$$

$$\delta\alpha_T = \arccos\frac{-\mathbf{k}'_T \cdot \delta\mathbf{p}_T}{k'_T\delta p_T},$$

$$\delta\phi_T = \arccos\frac{-\mathbf{k}'_T \cdot \mathbf{p}_T^N}{k'_T p_T^N},$$

$$(22)$$

where $\mathbf{k}'_T$ and $\mathbf{p}_T^N$ are, respectively, the projections of the final lepton and nucleon momentum on the transverse plane (if the neutrino direction is taken as the z axis, then the projections only have components in the xy plane). In the PWIA, for which $\mathbf{k'} + \mathbf{p}_N = \mathbf{k} + \mathbf{p}_m$, $\delta\mathbf{p}_T$ is the transverse component of the initial nucleon momentum, and $\delta\alpha_T$ is the angle between the transverse projections of the initial nucleon momentum and the transferred momentum $\mathbf{q}$. As shown in Ref. [30], in the PWIA limit, the $\delta\alpha_T$ distribution is expected to be flat due to the isotropy property shown by the nucleon momentum distribution (Fermi motion). This result will be discussed in detail for the different nuclear models and different experimental kinematics in the next section. The presence of FSIs and other effects beyond the impulse approximation break this behavior (work along this line is presently in progress [32]).
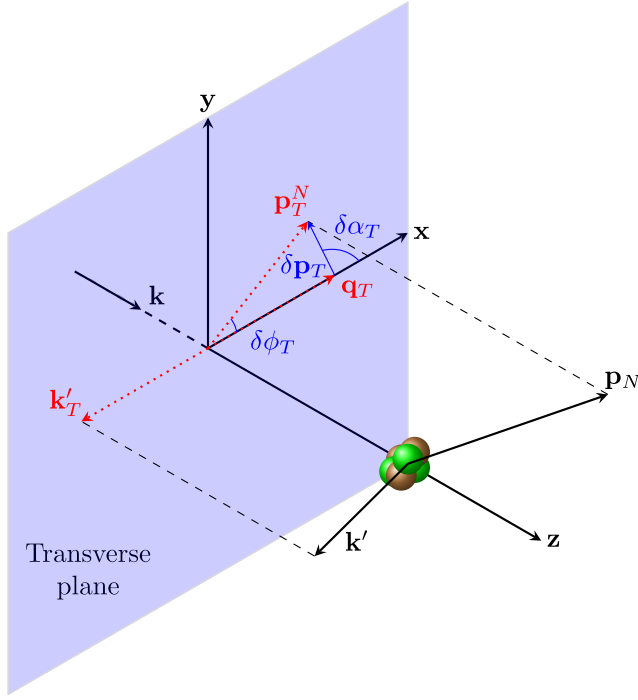
FIG. 3. Scheme showing TKI: δp_T, $\delta \alpha_T$, and $\delta \phi_T$. The final lepton and nucleon momenta are projected on the plane perpendicular to the neutrino direction (*xy* plane or transverse plane). The transverse component of the transferred momentum ($\mathbf{q}_T$) equals $-\mathbf{k}'_T$ and defines the *x* axis.

The T2K and MINERνA collaborations measured single differential cross sections with respect to TKI defined in Eq. (22). These can be calculated by integrating the sixth-differential semi-inclusive cross section in Eq. (1), given in terms of the NV, over five of the six variables, after performing the appropriate change of variables. Hence, to compare with these data, we need to connect the two sets of variables and evaluate the necessary Jacobians. The details of these transformations are given in the Appendix, leading to the expressions

$$
\frac{d\sigma}{d\delta p_T} = 2\pi \int_{\theta_l^{\min}}^{\theta_l^{\max}} d\theta_l \sin\theta_l \int_{k'_{\min}}^{k'_{\max}} dk' \int_{\theta_N^{L\min}}^{\theta_N^{L\max}} d\theta_N^L \sin\theta_N^L
$$
$$
\times \int_{\phi_N^{L\min}}^{\phi_N^{L\max}} d\phi_N^L \langle d^5\sigma \rangle \mathcal{J}_p \Theta(p_N - p_N^{\min}) \Theta(p_N^{\max} - p_N),
$$
$$
(23)
$$

$$
\frac{d\sigma}{d\delta \alpha_T} = 2\pi \int_{\theta_l^{\min}}^{\theta_l^{\max}} d\theta_l \sin\theta_l \int_{k'_{\min}}^{k'_{\max}} dk' \int_{p_N^{\min}}^{p_N^{\max}} dp_N
$$
$$
\times \int_{\phi_N^{L\,\min}}^{\phi_N^{L\,\max}} d\phi_N^L \langle d^5\sigma \rangle \mathcal{J}_\alpha \sin\theta_N^L \Theta(\theta_N^L - \theta_N^{L\,\min})
$$
$$
\times \Theta(\theta_N^{L\,\max} - \theta_N^L),
$$
$$
(24)
$$

$$
\frac{d\sigma}{d\delta \phi_T} = 2\pi \int_{\theta_l^{\min}}^{\theta_l^{\max}} d\theta_l \sin\theta_l \int_{k'_{\min}}^{k'_{\max}} dk' \int_{p_N^{\min}}^{p_N^{\max}} dp_N
$$
$$
\times \int_{\theta_N^{L\,\min}}^{\theta_N^{L\,\max}} d\theta_N^L \langle d^5\sigma \rangle \sin\theta_N^L,
$$
$$
(25)
$$

where $\langle d^5\sigma \rangle$ is the flux-averaged fifth-differential semi-inclusive cross section

$$
\langle d^5\sigma \rangle = \left\langle \frac{d\sigma}{dk' d\Omega_{k'} dp_N d\Omega_N^L} \right\rangle
$$
$$
(26)
$$

and the Jacobians $\mathcal{J}_p$ and $\mathcal{J}_\alpha$ have been defined, respectively, in Eq. (A4) and Eq. (A8). The integration limits are either dictated by the kinematics or imposed by the experimental cuts, as will be shown in results section.

C. Inferred variables

The T2K Collaboration also measured [17] single differential cross sections as function of the so-called inferred variables, which compare the momentum and angle of the ejected proton with the proton kinematics inferred from the measured final muon kinematics under the so-called QE hypothesis, i.e., initial nucleon at rest. In this approximation, the neutrino energy and the final proton momenta are defined as

$$
E_\nu = \frac{m_p^2 - m_l^2 + 2E_l(m_n - E_b) - (m_n - E_b)^2}{2[m_n - E_b - E_l + k' \cos\theta_l]}
$$
$$
(27)
$$

and

$$
\mathbf{p}_N^{\inf} = (-k' \sin\theta_l, 0, -k' \cos\theta_l + E_\nu),
$$
$$
(28)
$$

where the *z* axis corresponds to the neutrino direction; m_n, m_p, and m_l are the neutron, proton, and muon masses; and E_b and E_l are the nuclear binding energy fixed to 25 MeV for ^{12}C and the muon energy. Then, when a muon and (at least) one proton are measured in the final state, we can define three observables,

$$
\Delta p = |\mathbf{p}_N| - |\mathbf{p}_N^{\inf}|,
$$
$$
\Delta \theta = \theta_N^L - \theta_N^{\inf},
$$
$$
|\Delta \mathbf{p}| = |\mathbf{p}_N - \mathbf{p}_N^{\inf}|,
$$
$$
(29)
$$

with $\mathbf{p}_N$ the 3-momentum of the ejected nucleon, θ_N^L the angle between the final nucleon and the direction of the incoming neutrino, and $\theta_N^{\inf}$ the angle between the neutrino direction and the 3-momentum of the ejected nucleon in the QE hypothesis defined as

$$\cos\theta_N^{\mathrm{inf}} = \frac{\mathbf{p}_N^{\mathrm{inf}} \cdot \mathbf{z}}{|\mathbf{p}_N^{\mathrm{inf}}|} = \frac{-k'\cos\theta_l + E_\nu}{|\mathbf{p}_N^{\mathrm{inf}}|}. \tag{30}$$

The definition (29) of $|\Delta\mathbf{p}|$ can be expressed as a second-degree equation for p_N in the form $p_N^2 + 2b'p_N + c' = 0$ as follows:

$$p_N^2 + 2p_N(k'\sin\theta_N^L\cos\phi_N^L\sin\theta_l - E_\nu\cos\theta_N^L + k'\cos\theta_N^L\cos\theta_l) + k'^2\sin^2\theta_l + (k'\cos\theta_l - E_\nu)^2 - |\Delta\mathbf{p}|^2 = 0. \tag{31}$$

Notice that, according to Eqs. (28) and (30), the definition of the inferred proton kinematics relies on the same QE expression used, for example, in the estimation of neutrino energy at T2K oscillation measurements. Consequently, the observed deviations from the expected proton inferred kinematic imbalance could provide hints of the biases that may be caused from the mismodeling of nuclear effects in neutrino oscillation measurements at T2K [17].

For the inferred variables, the single differential cross sections can be defined following the same procedure used with TKI in the previous section, yielding

$$\frac{d\sigma}{d\Delta p} = 2\pi \int_{\theta_l^{\min}}^{\theta_l^{\max}} d\theta_l \, \sin\theta_l \int_{k'_{\min}}^{k'_{\max}} dk' \int_{\theta_N^{L\min}}^{\theta_N^{L\,\max}} d\theta_N^L \, \sin\theta_N^L \int_{\phi_N^{L\,\min}}^{\phi_N^{L\,\max}} d\phi_N^L \langle d^5\sigma\rangle \Theta(p_N - p_N^{\min})\Theta(p_N^{\max} - p_N),$$

$$\frac{d\sigma}{d\Delta\theta} = 2\pi \int_{\theta_l^{\min}}^{\theta_l^{\max}} d\theta_l \sin\theta_l \int_{k'_{\min}}^{k'_{\max}} dk' \int_{p_N^{\min}}^{p_N^{\max}} dp_N \int_{\phi_N^{L\,\min}}^{\phi_N^{L\,\max}} d\phi_N^L \langle d^5\sigma\rangle \sin\theta_N^L \Theta(\theta_N^L - \theta_N^{L\,\min})\Theta(\theta_N^{L\,\max} - \theta_N^L),$$

$$\frac{d\sigma}{d|\Delta\mathbf{p}|} = 2\pi \int_{\theta_l^{\min}}^{\theta_l^{\max}} d\theta_l \sin\theta_l \int_{k'_{\min}}^{k'_{\max}} dk' \int_{\theta_N^{L\,\min}}^{\theta_N^{L\,\max}} d\theta_N^L \sin\theta_N^L \int_{\phi_N^{L\,\min}}^{\phi_N^{L\,\max}} d\phi_N^L \langle d^5\sigma\rangle \mathcal{J}_{\Delta\mathbf{p}}\Theta(p_N - p_N^{\min})\Theta(p_N^{\max} - p_N), \tag{32}$$

with $\mathcal{J}_{\Delta\mathbf{p}}$ the Jacobian of the variable change $p_N \to |\Delta\mathbf{p}|$,

$$\mathcal{J}_{\Delta\mathbf{p}} = \left|\frac{\partial p_N}{\partial|\Delta\mathbf{p}|}\right|_{(\theta_N,\phi_N)} = \left|\frac{\Delta\mathbf{p}}{p_N + b'}\right|. \tag{33}$$

As it happened for TKI, also in this case, the second-degree equation (31) can have (see Appendix) zero, one, or two valid solutions in the variable p_N (namely, belonging to the interval $[p_N^{\min}, p_N^{\max}]$). In the latter case, the contributions from both solutions must be summed.

IV. RESULTS

In this section, we compare our theoretical results based on the PWIA with CC0π measurements of three neutrino collaborations: T2K, MINERνA, and MicroBooNE. For each experiment, we compare our predictions with inclusive single or double differential cross sections as function of the muon momentum and scattering angle. Next, we show the semi-inclusive cross section results (CC0π1p where a muon and a proton are detected in the final state) as function of NV, IV, or TKI depending on the available data from each experiment. As it was explained in Sec. III, the main ingredient of our theoretical calculations is the flux-averaged fifth-differential semi-inclusive cross section function of the independent variables $(k', \theta_l, p_N, \theta_N^L, \phi_N^L)$. To compare with experimental data, usually given as single or double differential cross sections, we need to perform the appropriate change of variables, if it applies, and integrate numerically. All the theoretical results presented in this work were obtained by combining trapezoid and Gaussian quadrature integration methods.

A. T2K

The T2K data sample [17] includes CC0π inclusive cross sections without protons in the final state as a function of final muon variables and CC0π1p semi-inclusive cross sections with at least one proton and one muon in the final state as function of NV, IV, and TKI. The phase-space restrictions applied to the analyses as a function of each set of variables are summarized in Table I.

Starting with the CC0π data, in Fig. 4, we show the flux-averaged differential inclusive cross sections for ^{12}C evaluated for the three nuclear models considered, RFG (blue dashed), IPSM (solid red), and NO (green dot-dashed). Note that, as specified in Table I, only the outgoing protons with momentum $p_N < 0.5$ GeV contribute to the experimental signal. Accordingly, only these events are

TABLE I. Final muon and proton phase-space restrictions applied to the CC0π data shown by T2K Collaboration in Ref. [17].

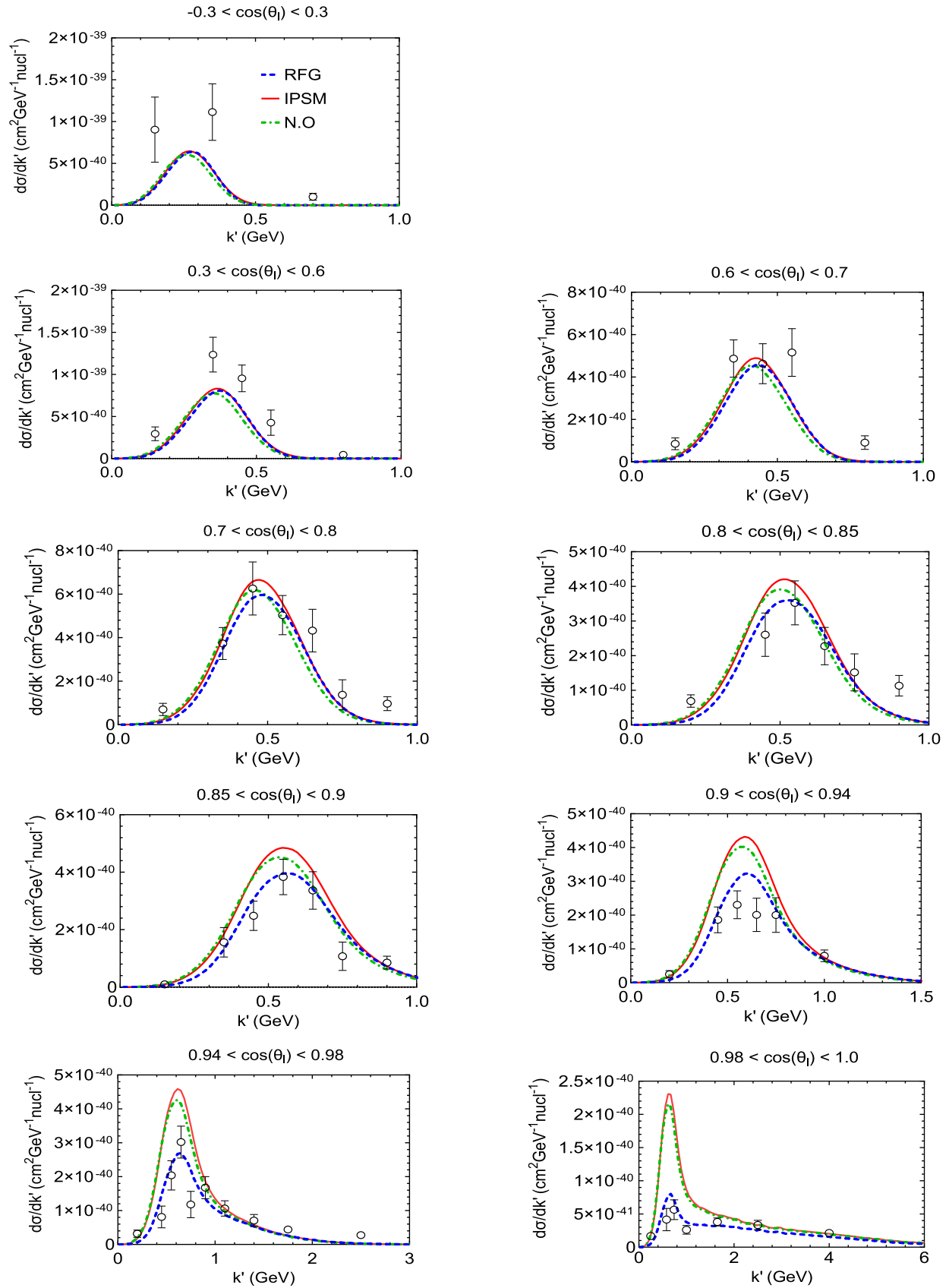| T2K	k'	$\cos\theta_l$	p_N	$\cos\theta_N^L$	ϕ_N^L
Inclusive NV	$\cdots$	$\cdots$	<0.5 GeV	$\cdots$	$\cdots$
Semi-inclusive NV	$\cdots$	$\cdots$	>0.5 GeV	$\cdots$	$\cdots$
TKI	>0.25 GeV	> -0.6	0.45–1.0 GeV	>0.4	$\cdots$
IV	$\cdots$	$\cdots$	>0.45 GeV	>0.4	$\cdots$

FIG. 4.   The T2K CC0π inclusive $\nu_\mu - {}^{12}$C cross sections without protons in the final state with momenta above 0.5 GeV as a function of final muon kinematics for different nuclear models. Data taken from Ref. [17].
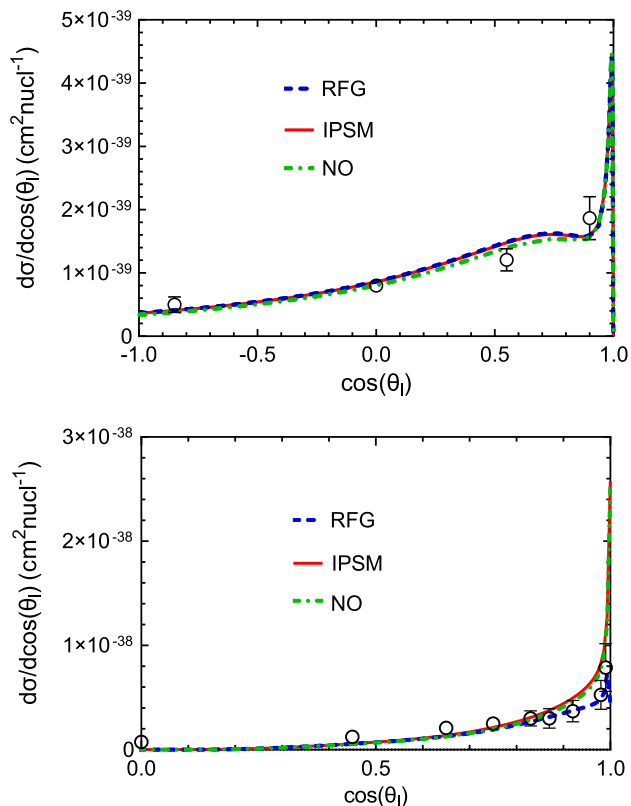
FIG. 5.   T2K inclusive cross sections as function $\cos\theta_l$ obtained after integrating over all protons in the final state with momenta above 0.5 GeV (top panel) and with momenta below 0.5 GeV (bottom panel). Data taken from Ref. [17].

considered in the theoretical calculations performing the integral over p_N with an upper limit of integration equal to 0.5 GeV. Despite the very different momentum distributions for the three models, particularly for RFG, the corresponding inclusive cross sections are rather similar for $\cos\theta_l$ smaller than about 0.8, becoming more and more different from each other as the scattering angle approaches zero (i.e., small transferred energy), where the IPSM and NO results are much higher than the data, whereas the RFG ones stay close to the data. As discussed in Refs. [33–35], the PWIA approach fails to describe lepton-nucleus scattering reactions at low values of the momentum and energy transfers. This is a consequence of the lack of orthogonality between the bound and free nucleon wave functions and of the large effects associated to the overlap between the initial and final states. As already noticed, for the RFG model, the cross section at very small scattering angles is reduced and compares better with the data. This is the effect of Pauli blocking, which is by definition included in the RFG model and implies that the ejected nucleon must obey $p_N > k_F$. We expect that the orthogonalization of the initial and final nuclear wave functions, as well as the implementation of FSI, will bring the IPSM and NO results closer to the data

even for the smaller scattering angles. Work along these lines is in progress [32].

In Fig. 5, we present the single differential inclusive cross section $d\sigma/d\cos\theta_l$ as a function of $\cos\theta_l$ when the integral over momenta of the ejected nucleon $p_N < 0.5$ GeV is performed (bottom panel) or restricting the analysis to $p_N > 0.5$ GeV (top panel). Comparing the two results, we can see that the difference between the RFG and the other two models for θ_l close to zero observed for $p_N < 0.5$ GeV is not present for $p_N > 0.5$ GeV. This is a result of imposing a minimum value of the final proton momentum, which is somehow equivalent to include Pauli blocking effects, because the orthogonality problem of the two shell models is hidden in this case by the experimental constraint on the final proton momentum.

Moving now to the $CC0\pi1p$ data, in Fig. 6, we present single differential semi-inclusive $\nu_\mu - {}^{12}C$ cross sections with respect to the NV for the three nuclear models compared with available T2K data. Two different kinds of cross sections are considered: in the two top rows, cross sections are presented as functions of $\cos\theta_N^L$ in bins of $\cos\theta_l$, and in the two bottom rows, they are presented as functions of p_N in bins of $\cos\theta_l$ and $\cos\theta_N^L$. In all cases, p_N is larger than 0.5 GeV (see Table I). As shown, the uncertainty connected with the nuclear model is, in general, small and comparable with the one obtained for inclusive cross sections, taking into account that the experimental constraints imposed mask the orthogonality problem of the two shell models in the low-q area.

In general, the interpretation of the discrepancies and agreements between our results and the data shown in Figs. 4, 5, and 6 is not straightforward since the measured cross sections are affected by multiple initial and final nuclear state effects which cannot be easily separated in the momentum and angular kinematic distributions. Note that the theoretical results presented here only include the quasielastic regime and are based on the PWIA, neglecting FSI and 2p2h contributions, which will be implemented in future work. A hint about the effects of these corrections is offered by simulations performed using the NEUT generator shown in Ref. [17], in which the different effects of adding FSI and 2p2h, as included in this generator, are displayed. From this analysis, it is shown that FSIs increase the events without any proton with momentum above 0.5 GeV, thus enlarging the cross sections shown in Figs. 4 and 5 (bottom panel) and decreasing the cross sections shown in Figs. 6 and 5 (top panel). The second (2p2h), according to the NEUT simulation, affects equally inclusive and semi-inclusive events by increasing the cross sections, but as also happens for FSI, the effects for different bins can be very different. In our model, the complexity of the calculations makes it difficult to predict how the cross sections will be modified by FSI and/or 2p2h before detailed calculations with strong
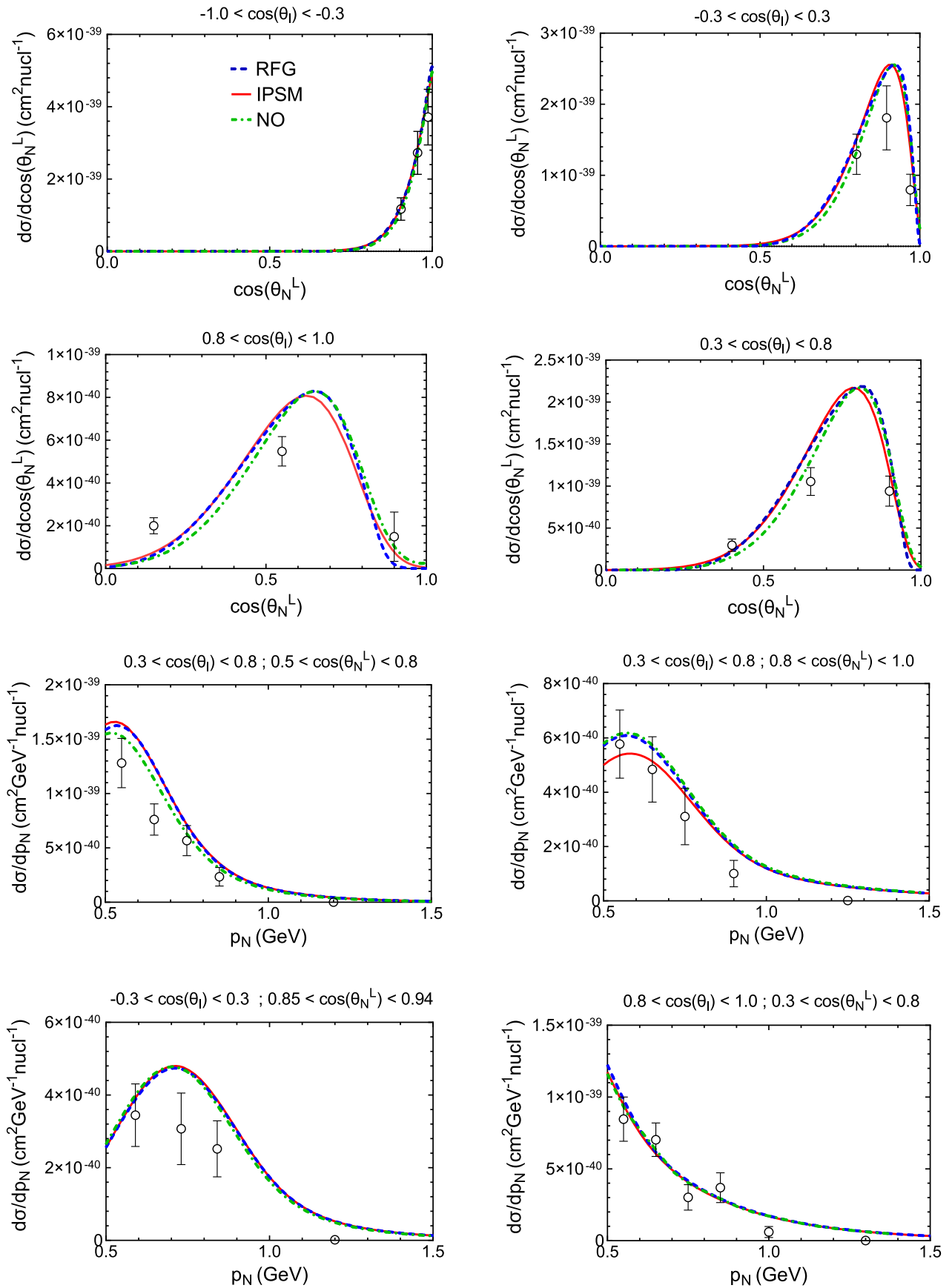
FIG. 6.   The T2K CC0π1p single differential $\nu_\mu - ^{12}$C cross sections as function of the NV. Data taken from Ref. [17].
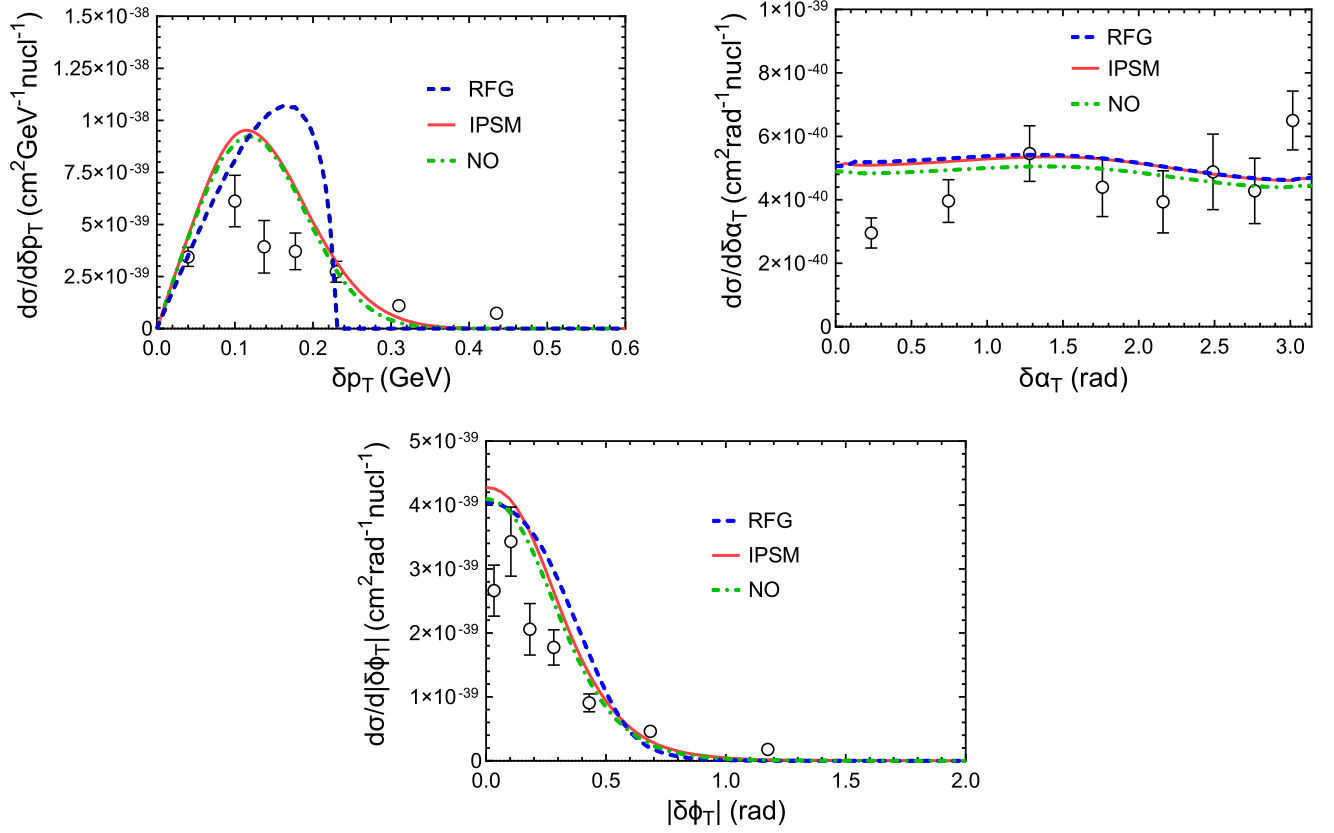
FIG. 7. The T2K CC0π1p single differential $\nu_\mu - ^{12}$C cross sections as function of the transverse kinematic imbalances δp_T, $\delta\alpha_T$, and $|\delta\phi_T|$ for the RFG model (blue dashed), IPSM (red solid), and NO (green dot-dashed). Data taken from Ref. [17].

relativistic scalar and vector potentials in the final state are performed (work in progress).

Next, we analyze the data in terms of the transverse kinematic imbalances defined in Eq. (22). In Fig. 7, we show the semi-inclusive cross sections as function of TKI compared with the T2K data. As explained in Sec. III B, this set of variables is designed to minimize the dependence on neutrino energy [30]. Only for $\delta\phi_T$, results are shown to depend more strongly on the kinematics of the incoming neutrino [31]. In the absence of FSI, the momentum imbalance is generated entirely by the description of the initial nuclear state dynamics. In this approximation, δp_T is a direct measurement of the transverse component of the bound nucleon momentum distribution. As can be seen in the top panel of Fig. 7, the RFG cross section $d\sigma/d\delta p_T$ differs strongly from the other two, not only in magnitude and position of the maximum but also in the fact that the RFG distribution vanishes for $\delta p_T > k_F$ as a consequence of the Fermi condition. Although the position of the peak looks correct for the IPSM and NO models, the corresponding results overestimate the data in the low δp_T area (below the Fermi momentum located around 0.23 GeV for ^{12}C) and underestimate the data for high δp_T, indicating that effects beyond PWIA might be essential to correctly describe the data. In the middle panel of Fig. 7, we show the

cross sections as a function of $\delta\alpha_T$. In this case, the NO prediction is a bit smaller than the RFG and IPSM ones, but all models exhibit a flat distribution as was expected due to the PWIA and the isotropy of the associated momentum distributions. As it happened with δp_T, for $\delta\alpha_T$, we also see that PWIA is inadequate to describe the data. The inclusion of FSI and 2p2h contributions will likely improve the agreement with data. Finally, we also present the $|\delta\phi_T|$ distributions in the bottom panel of Fig. 7, showing few discrepancies between the different models except for slightly smaller values of the cross sections around $|\delta\phi_T| = 0$ for the RFG and NO models and a wider distribution for RFG compared with the other two models. As happened with the other TKI, the PWIA does not give a good quantitative description of the data, although in this case it reproduces correctly the shape of the cross section.

To conclude with T2K analysis, in Figs. 8, 9, and 10, we present the semi-inclusive cross sections as functions of the inferred variables Δp, $\Delta\theta$, and $|\Delta\mathbf{p}|$ in different regions distinguished by a specific bin of muon kinematics. The discrepancies between the different nuclear models depend on the particular kinematics considered and are larger for low values of the muon kinematic bin. Note that the region of forward scattering angles refers to low values of the energy and momentum transferred in the process. In this
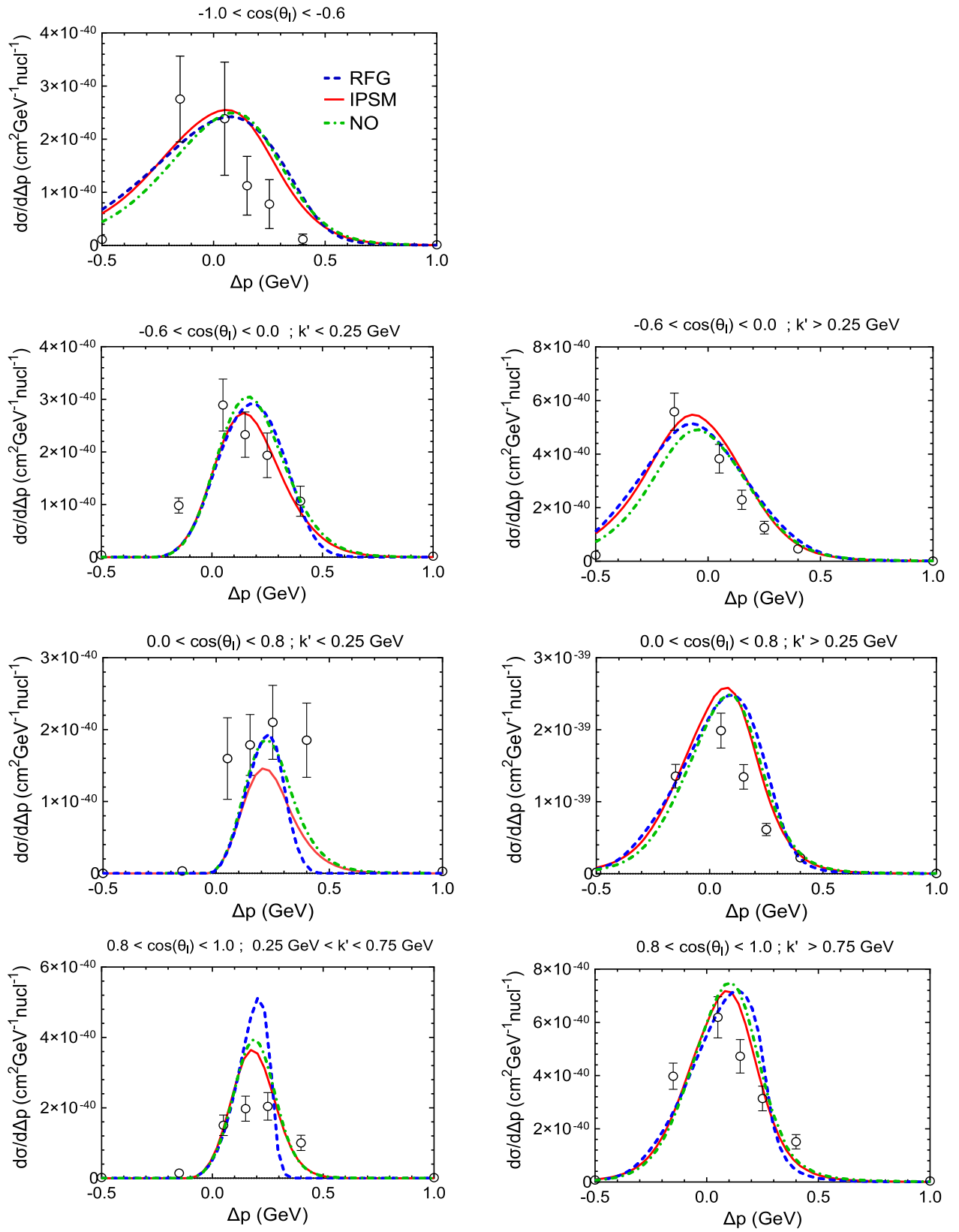
FIG. 8.   T2K CC0π1p single differential $\nu_\mu - {}^{12}$C cross section as function of Δp in different muon kinematic bins with constrains of the proton kinematics given in Table I for the RFG (blue dashed), IPSM (red solid) and NO (green dot-dashed) nuclear models. Data taken from [17].
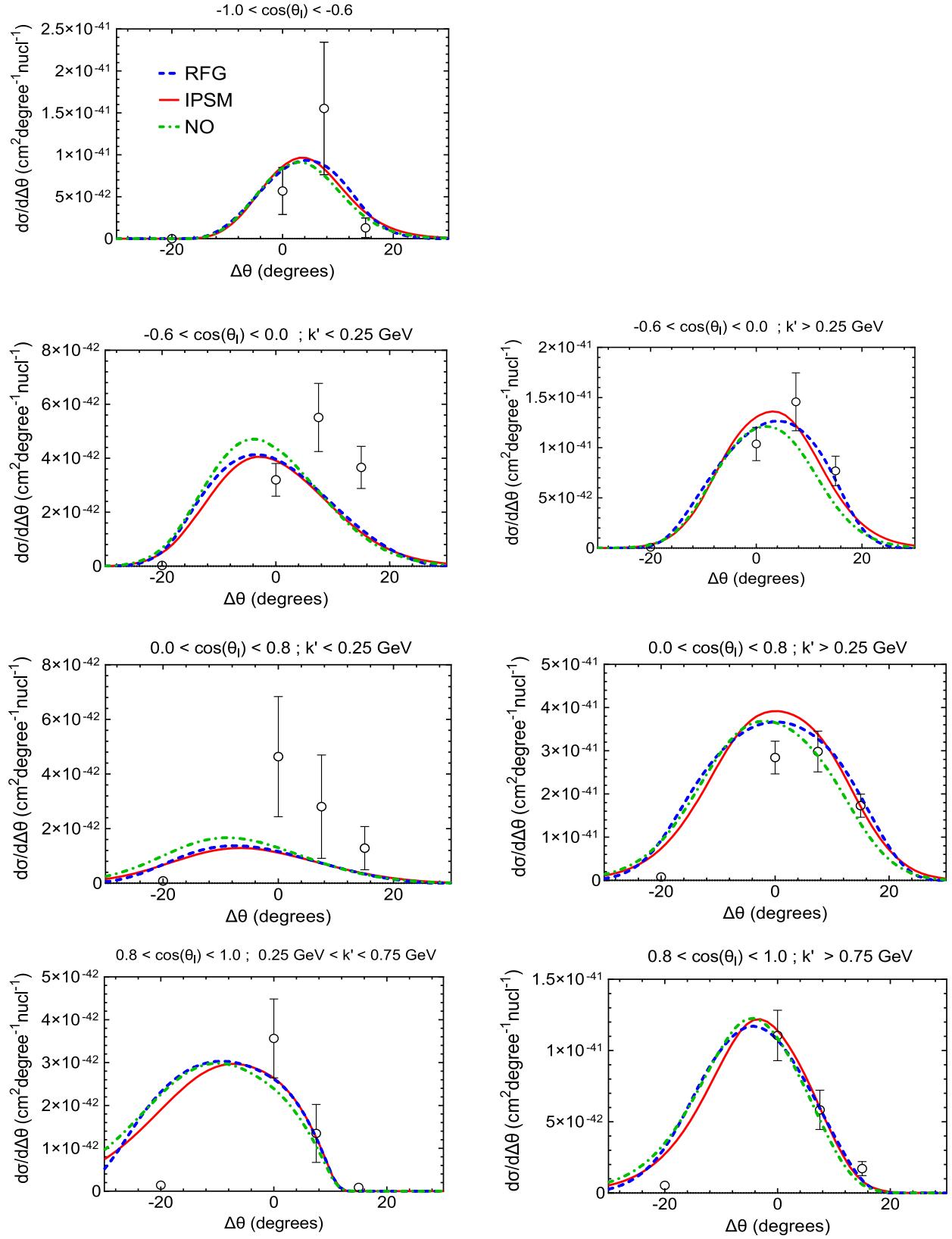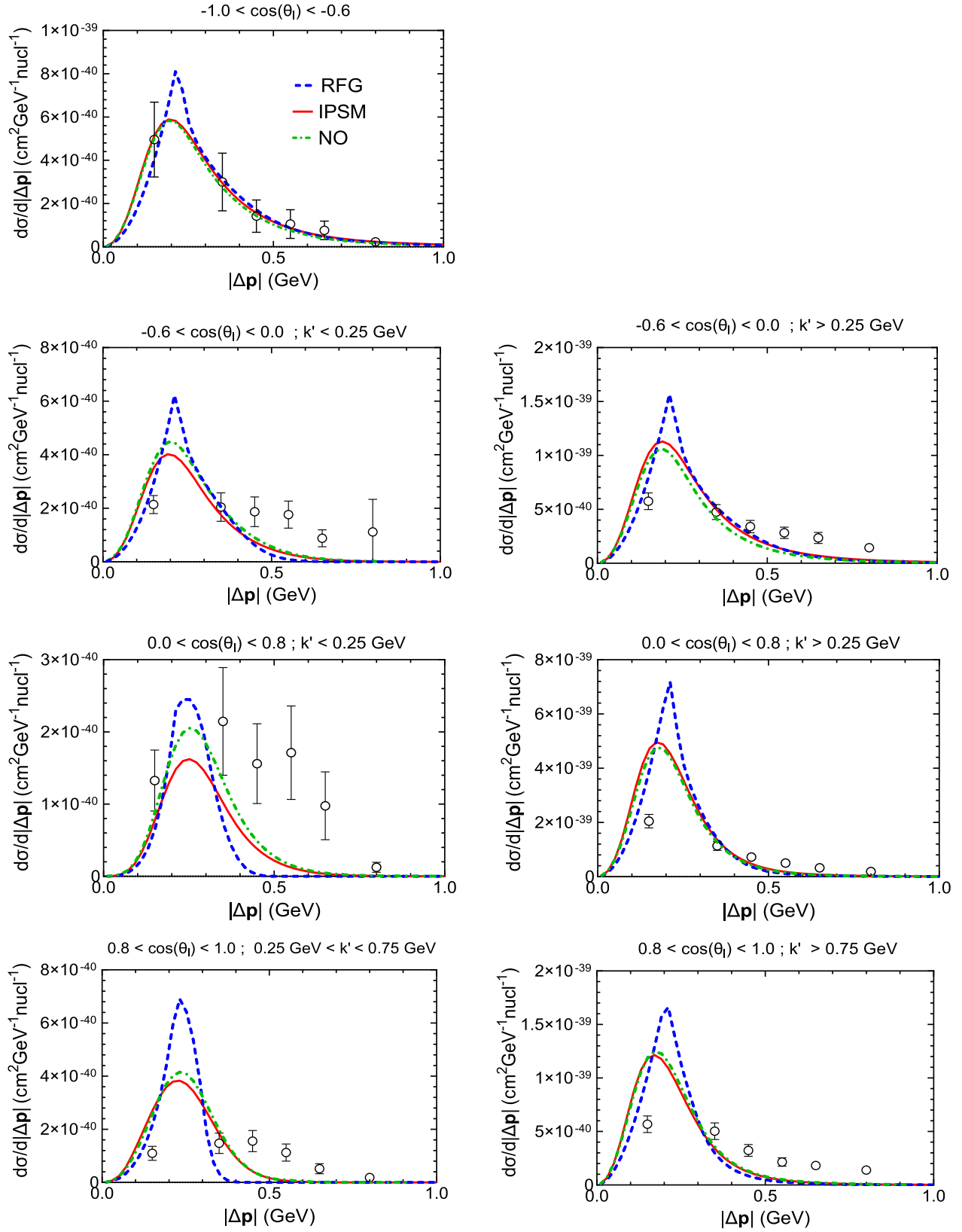
FIG. 9.   The T2K CC0π1p single differential $\nu_\mu -^{12}$ C cross section as function of $\Delta\theta$ in different muon kinematic bins with constrains of the proton kinematics given in Table I for the RFG (blue dashed), IPSM (red solid), and NO (green dot-dashed) nuclear models. Data taken from Ref. [17].

FIG. 10. The T2K CC0π1p single differential $\nu_\mu - {}^{12}$C cross section as function of $|\Delta\mathbf{p}|$ in different muon kinematic bins with constrains of the proton kinematics given in Table I for the RFG (blue dashed), IPSM (red solid), and NO (green dot-dashed) nuclear models. Data taken from Ref. [17].

TABLE II.   Final muon and proton phase-space restrictions applied to the CC0π data shown by the MINERνA Collaboration in Refs. [18,19]. Note that, in contrast with what the T2K Collaboration does in Ref. [17], for MINERνA the same restrictions are applied to the analyses of the single differential cross sections as function of any kind of variables, i.e., NV and TKI.

MINERνA	k'	$\cos\theta_l$	p_N	$\cos\theta_N^L$	ϕ_N^L
All analyses	1.5–10 GeV	>0.939	0.45–1.2 GeV	>0.342	⋯

kinematical situation, the predictions based on the impulse approximation are questionable, and ingredients related to low-energy nuclear effects such as binding energies, Pauli blocking, nucleon off-shell-ness, and collective effects can be more relevant. In particular, this can be noticed in the cases of Δp (left panels in Fig. 8) and $|\Delta \mathbf{p}|$ (Fig. 10). In the latter, the discrepancy between the RFG and the IPSM/NO models is remarkable. A similar comment applies also to some specific kinematics in Fig. 8. On the contrary, the three models lead to rather similar results for the cross section as a function of $\Delta\theta$ (Fig. 9). Our predictions are consistent with the simulations shown in Ref. [17] for those kinematical regions where effects beyond the impulse approximation and FSI are expected to be minor. This

corresponds to the quasielastic peak and sufficiently high values of the transferred energy/momentum. This is clearly illustrated in the results shown where some kinematics are very well described by the model, even being based on PWIA, whereas some other situations are completely off. The latter correspond to kinematics where the simulations show larger effects due to FSI and ingredients beyond the impulse approximation. However, this analysis should be verified by further theoretical calculations [32] where, among other ingredients, FSI effects will be addressed using different descriptions for the relativistic nuclear potentials. The present study should be considered as a first step in providing a consistent comparison between data and a microscopic theoretical description of semi-inclusive neutrino-nucleus scattering reactions.

B. MINERνA

Moving now to the comparison with the results presented by the MINERνA Collaboration, in Table II, we summarize the constraints in the kinematics of the final muon and proton applied to the data published in Refs. [18,19]. In this case, we compare our results as function of NV and TKI with the latest available data from the MINERνA experiment.

In Fig. 11, we show the inclusive cross sections as function of the final muon momentum and scattering
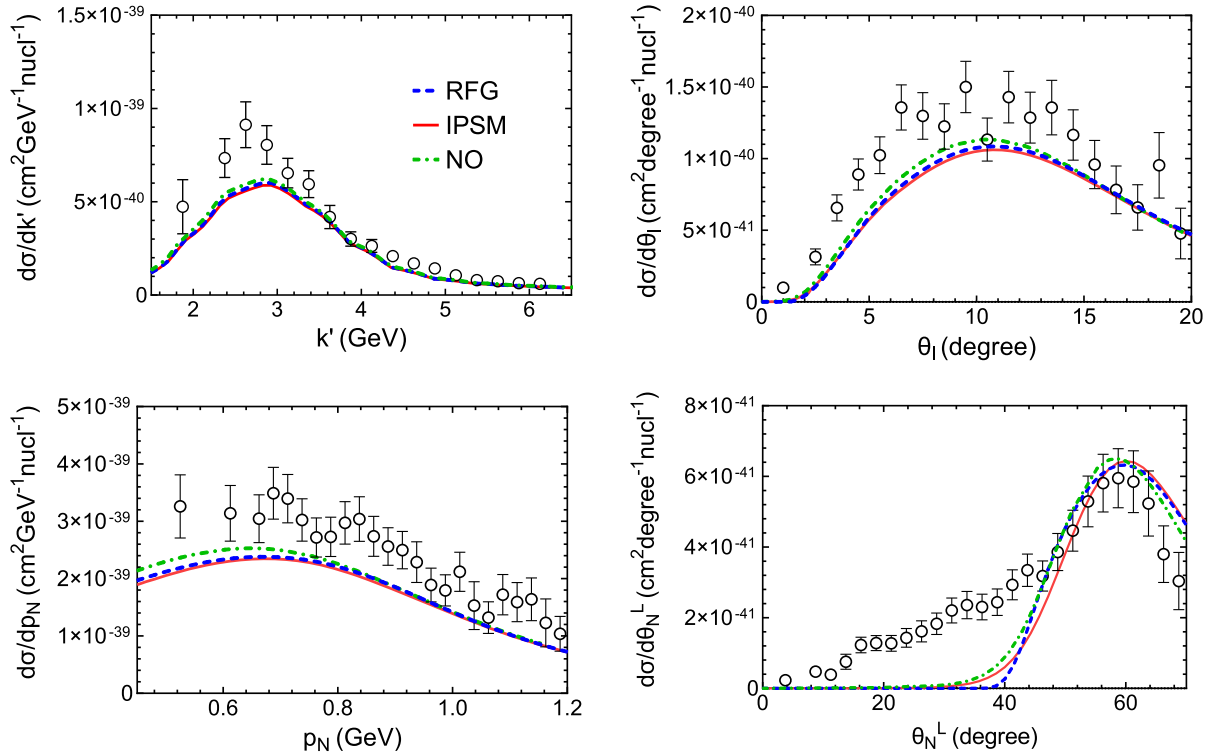

FIG. 11.   The MINERνA single differential inclusive $\nu_\mu - {}^{12}$C cross sections as a function of the final muon momentum and scattering angle (top) and as a function of the final proton momentum and polar angle (bottom) for the RFG (blue dashed), IPSM (red solid), and NO (green dot-dashed) nuclear models. The original paper with MINERνA data was Ref. [18], but the data shown here were taken from Ref. [19], which corrected a mismodeling in GENIE's elastic FSI that affected the experimental data presented in the first paper.
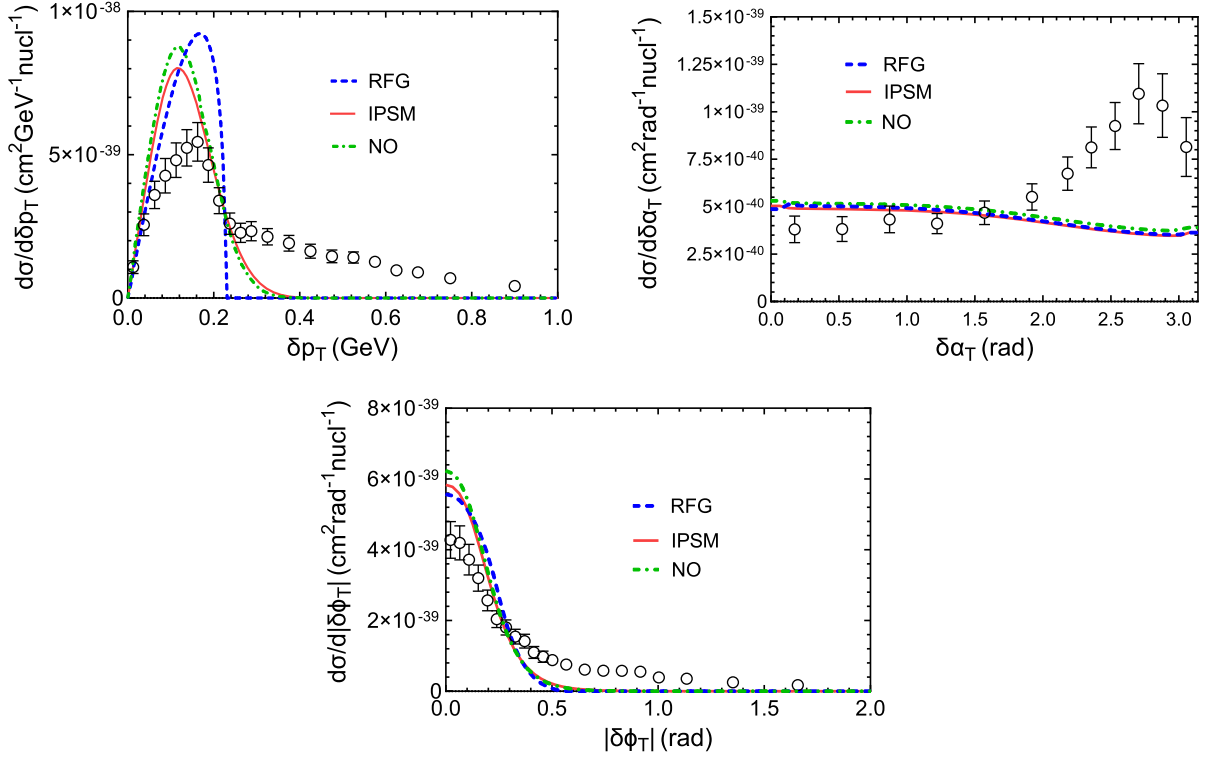
FIG. 12. The MINERνA CC0π1p single differential $\nu_\mu - {}^{12}$ C cross sections as function of the transverse kinematic imbalances δp_T, $\delta\alpha_T$, and $|\delta\phi_T|$ for the RFG (blue dashed), IPSM (red solid), and NO (green dot-dashed) nuclear models. The original paper with MINERνA TKI data was Ref. [18], but the data shown here were taken from Ref. [19], which corrected a mismodeling in GENIE's elastic FSI that affected the experimental data presented in the first paper.

angle (top) and as function of the proton momentum and polar angle (bottom) for the three nuclear models considered. There is not any significant difference between the results in PWIA using the different nuclear models. In addition to this, our results reproduce very well the results generated by GENIE without FSI included in Ref. [18], but systematically fall below the data. As pointed out in Ref. [18], missing ingredients beyond the PWIA are

necessary to describe correctly the experimental data, with a special mention to the area below $\theta_N^L \approx 40°$ where pion emission and reabsorption and 2p2h are, according to the GENIE simulation, the main ingredients that contribute to the large and long tail appreciated in the data.

In Fig. 12, we present the differential cross sections as a function of TKI compared with MINERνA data. As we already observed for T2K, the δp_T distribution for the RFG
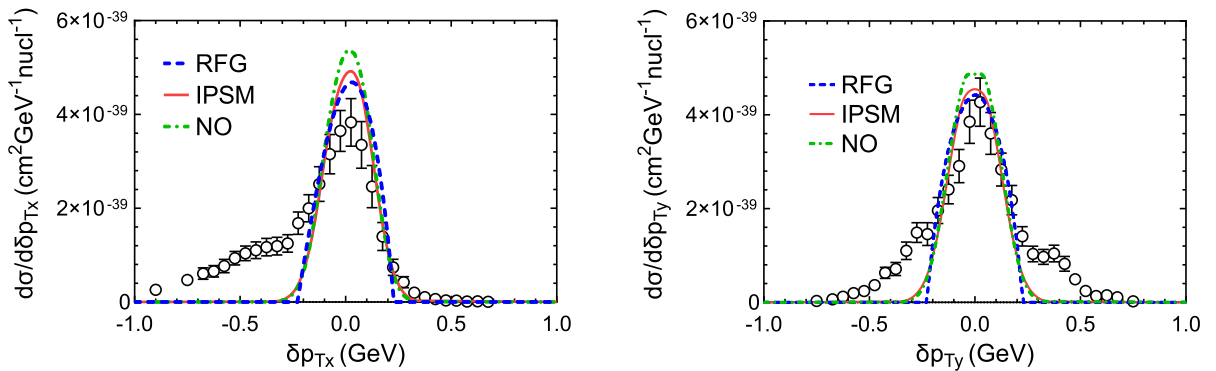

FIG. 13. The MINERνA CC0π1p single differential $\nu_\mu - {}^{12}$ C cross sections as a function of the projections of δp_T in the x axis (left) and in the y axis (right) for the RFG model (blue dashed), IPSM (red solid), and NO (green dot-dashed). Data taken from Ref. [19]. Notice that the convention used in Ref. [19] to define the x and y axis is the opposite of the convention used in this paper to define them, which is shown in Fig. 3.

TABLE III.   Muon and proton phase-space restrictions applied to the CC0π data shown by MicroBooNE collaboration in Refs. [20] (MicroBooNE A) and [21] (MicroBooNE B). Here, $\Delta\theta_{l,N}$ is the opening angle defined as the angle between the muon and the proton, and δp_T is the momentum imbalance in the transverse plane defined in Eq. (22).

MicroBooNE A	k'	$\cos\theta_l$	p_N	$\cos\theta_N^L$	ϕ_N^L	$\Delta\theta_{l,N}$	δp_T
All analyses	>0.1 GeV	$\cdots$	0.3–1.2 GeV	$\cdots$	$\cdots$	$\cdots$	$\cdots$
MicroBooNE B							
All analyses	0.1–1.5 GeV	$-0.65 < \cos\theta_l < 0.95$	0.3–1.0 GeV	>0.15	145–215°	35–145°	$\delta p_T < 0.35$ GeV

model differs from the other two models in the position of the peak and strength. This was expected because the momentum distribution of the RFG model is very different compared with the other two and δp_T in the PWIA is the transverse component of the bound nucleon momentum distribution. Also, as observed for T2K, in this case, the $\delta\alpha_T$ distribution is flat, as expected in the PWIA. Simulations using GENIE shown in Ref. [18] shed light on the differences observed between the data and the PWIA results, which are attributed to effects beyond the PWIA. Finally, note the theoretical prediction compared with data in the case of the cross section as a function of $|\delta\phi_T|$. Whereas the PWIA overestimates data at low $|\delta\phi_T|$, the reverse occurs for increasing $|\delta\phi_T|$ where the tail shown by data is completely absent in the PWIA results.

MINERνA also measured cross sections versus the x and y projections of the momentum imbalance along the Cartesian coordinate system shown in Fig. 3. Following the definition given in Eq. (22), the x and y components of the 3-momentum imbalance are

$$\delta p_{Tx} = k' \sin\theta_l + p_N \sin\theta_N^L \cos\phi_N^L, \qquad (34)$$

$$\delta p_{Ty} = p_N \sin\theta_N^L \sin\phi_N^L. \qquad (35)$$

In Fig. 13, we compare our results for the differential cross sections as a function of the components of the momentum imbalance with MINERνA data. If the interaction occurred on a free nucleon, then we would expect a delta function at $\delta p_T = 0$ because the muon and proton final states would be perfectly balanced in that case, as required by momentum conservation. As shown in Fig. 3, the initial and final leptons are contained in the xz plane, and so is the momentum transferred by the incoming neutrino. Therefore, in the PWIA, δp_{Ty} does not depend on any leptonic variable [see Eq. (35)] and is exactly the projection
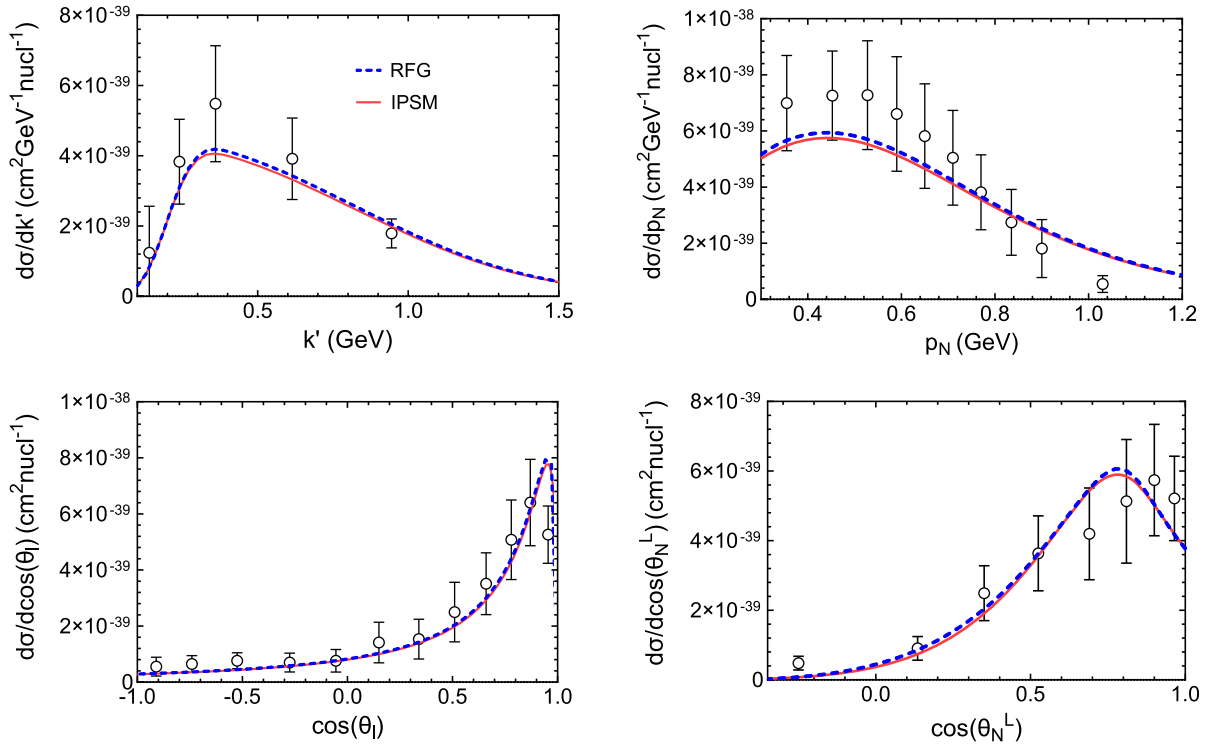

FIG. 14.   The semi-inclusive CC0π1p single differential $\nu_\mu - {}^{40}$Ar cross sections as function of final muon and proton kinematics for the MicroBooNE A dataset. Experimental data were taken from Ref. [20], and phase-space restrictions applied are summarized in Table III.
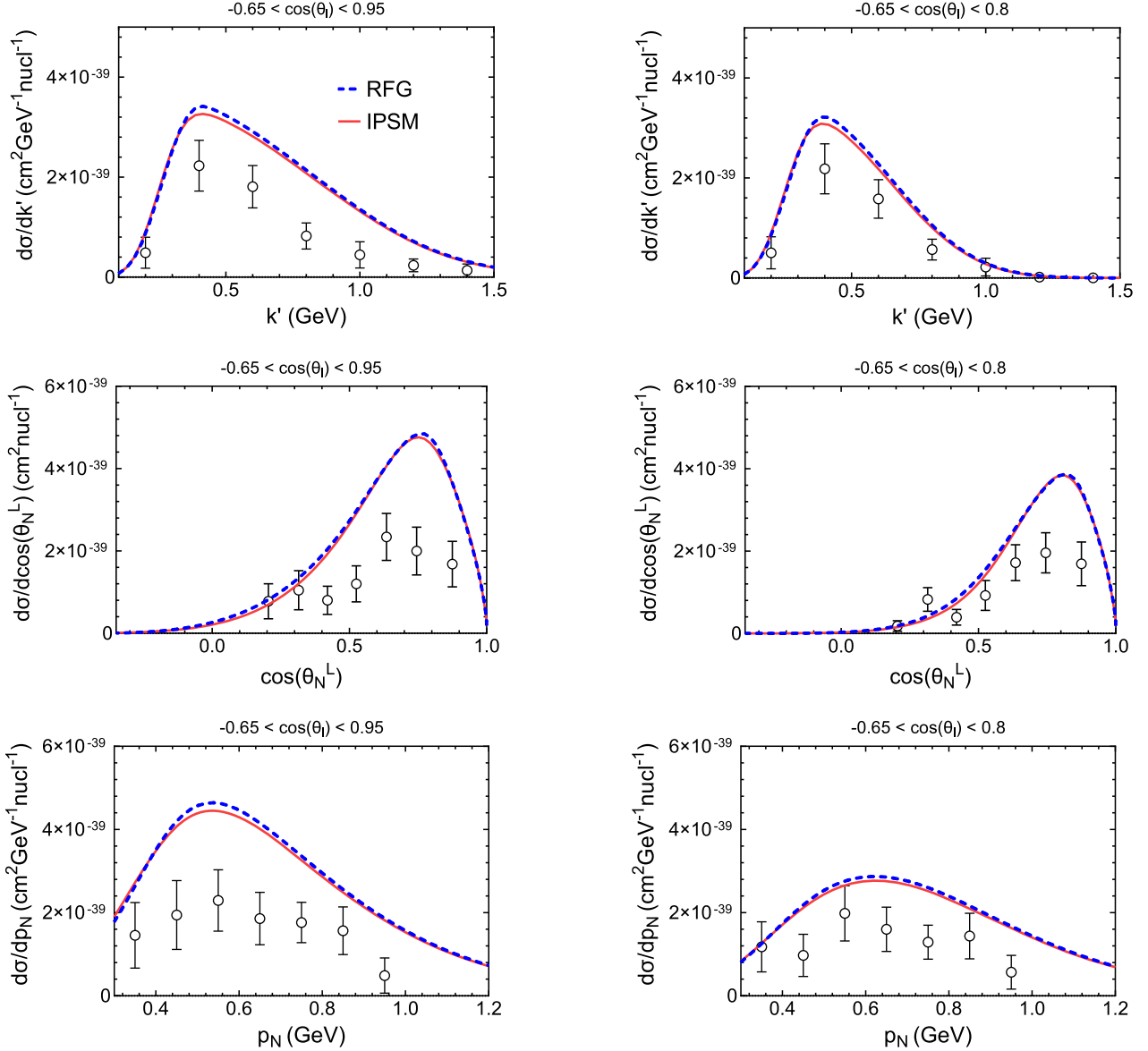
FIG. 15.   The semi-inclusive CC0π1p single differential $\nu_\mu - ^{40}$Ar cross sections as function of final muon and proton kinematics for the MicroBooNE B dataset. Experimental data were taken from Ref. [21], and phase-space restrictions applied are summarized in Table III.

on the y axis of the initial nucleon momentum. Because of the isotropy of the nucleon momentum distribution, the δp_{Ty} distributions obtained in Fig. 13 for all nuclear models are symmetrical around $\delta p_{Ty} = 0$, and the widths of the peaks are only the result of the Fermi motion. On the other hand, δp_{Tx} also depends on the final lepton kinematics, as seen in Eq. (34). This produces a very slight shift of the peaks toward positive values of δp_{Tx}. Results in the PWIA are able to reproduce correctly the position of the peak but fail to match the long tails appreciated in the experimental data and also overestimate some of the data around the peak. Contributions beyond PWIA may reduce the discrepancies observed in the present analysis.

C. MicroBooNE

In the previous sections, we have compared and analyzed experimental data of muon neutrinos on ^{12}C published by the T2K and MINERνA collaborations. The MicroBooNE Collaboration has also published CC0π1p flux-integrated differential cross sections of muon neutrinos on ^{40}Ar [20,21] as functions of the final particle momenta and angles. Next, we present results compared with two sets of experimental measurements published by MicroBooNE. The kinematic constraints imposed in the two measurements are summarized in Table III.

In Fig. 14, we show single differential $\nu_\mu - ^{40}$Ar cross sections as function of muon momentum and scattering

angle (left panels) and as function of proton momentum and polar angle (right panels) for two nuclear models, RFG and IPSM, compared with data shown in Ref. [20]. It is remarkable to point out how well the PWIA calculations reproduce the shape and magnitude of data. However, this does not contradict the important role that FSI and 2p2h contributions can play in the description of data for some kinematics according to GENIE simulations [20].

To go deeper in the analysis of MicroBooNE data, in Fig. 15, we present again single differential $\nu_\mu - {}^{40}$Ar cross sections as function of muon momentum and proton momenta and polar angle but now compared with experimental data shown in Ref. [21]. As explained there, the phase-space restrictions, which are summarized in Table III, were set to enhance CCQE interactions and to restrict the signal to the region where the detector response is well understood. Results are presented as a function of the muon momentum, the proton momentum, and polar angle, for two bins of $\cos\theta_l$, namely, $-0.65 < \cos\theta_l < 0.95$ (left panels) and $-0.65 < \cos\theta_l < 0.8$ (right panels).

Although both the RFG and the IPSM model overestimate the two sets of data, the disagreement is larger in the left plots, where the muon scattering angle reaches smaller values. This is because in both models the cross section peaks in the area defined by $0.8 < \cos\theta_l < 0.95$, as shown in Fig. 16. This region corresponds to low values of q and ω, and excluding the contribution of this small-θ_l zone will produce a reduction of the cross section. This is clearly observed by comparing theoretical predictions in the left and right panels in Fig. 15, and it is clearly in contrast with the data that only show a minor reduction when restricting the analysis to $\cos\theta_l < 0.8$. This different behavior of theoretical predictions and data is consistent with the significant discrepancy shown in Fig. 16 in the region of very small lepton scattering angles. A more careful study of this low-θ_l region is needed before more definite conclusions can be drawn.
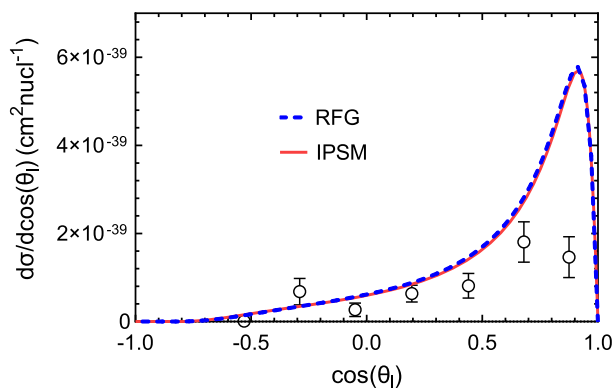

FIG. 16. The semi-inclusive CC0π1p single differential $\nu_\mu - {}^{40}$Ar cross sections as function of $\cos\theta_l$ for the MicroBooNE B dataset. Experimental data were taken from Ref. [21], and phase-space restrictions applied are summarized in Table III.

V. CONCLUSIONS

In this paper, we have analyzed all the available semi-inclusive CC0π experimental data where a muon and at least one proton are detected in the final state from T2K, MINERνA, and MicroBooNE neutrino collaborations. We have restricted ourselves to the plane wave impulse approximation; namely, ejected nucleons are described as plane waves, and only one-body current operators are considered. To describe the nuclear dynamics, we have used three different nuclear models: the relativistic Fermi gas, the independent-particle shell model with fully relativistic Dirac wave function, and the natural orbitals shell model which includes NN correlations.

Analytic expressions for the flux-averaged semi-inclusive cross sections for the three nuclear models are given as function of the momenta and angles of the muon and the proton detected in coincidence in the final state. Given that the experimental results were presented using different sets of kinematic variables, we have outlined the definition of each set, namely, transverse kinematic imbalances and inferred variables, and the explicit relationship between them and the final muon and proton momenta and angles measured in the laboratory system, denominated natural variables in this work.

Theoretical predictions for the cross sections as a function of the muon and proton momenta and angles show very little dependence upon the specific nuclear model used in the PWIA. Specifically for T2K, differences appreciated in Fig. 4 are related with the fact that IPSM and NO models produce a much larger cross section than the data in the low momentum and energy transferred in the PWIA. Great caution must be taken when looking at semi-inclusive results presented in Fig. 6 because, although it might look like the theoretical predictions describe correctly some of the data, FSI and 2p2h contributions are not included. It is important to notice that FSI effects may reduce the cross section at forward angles and low (q, ω) kinematics [35], being less relevant as one moves to higher (q, ω) values and backward angles. On the contrary, the absent 2p2h contributions may be approximately 15–25% of the cross section at low and intermediate kinematics [36]. Thus, the FSI and 2p2h contributions, not included in this work, can compensate each other at low-intermediate kinematics, producing similar results to the current ones based on PWIA. On the contrary, at higher kinematics, the effects of FSI are expected to be negligible, whereas the 2p2h contributions would increase the present results. More definite conclusions on the analysis will be drawn once these effects, FSI and 2p2h, are included in the general study (work in progress [32]). Accordingly, MINERνA results shown in Fig. 11 fall below the data for almost any value of the kinematic variables used. This difference can be attributed to contributions beyond PWIA [18]. In fact, the kinematics implied in MINERνA makes it possible to conclude that effects associated to FSI and 2p2h will be

crucial to improve the agreement with data. For MicroBooNE, results presented in Fig. 15 fall above the data even after excluding the contribution of $\cos\theta_\mu > 0.8$. We observe reductions of the cross sections similar to those obtained using Monte Carlo simulations when the events with $\cos\theta_\mu > 0.8$ are excluded, although the lack of effects beyond PWIA in our calculations does not allow us to find the root cause of the discrepancies between the results and the experimental data.

Concerning the use of variables linked with correlations between the muon and proton in the final state like the transverse kinematic imbalances, in the PWIA, δp_T is the projection in the transverse plane of the bound nucleon momentum; therefore, different momentum distributions will produce different δp_T distributions. As shown in Figs. 7, 12, and 13, the δp_T distributions obtained using the RFG model are different from the ones obtained using the other two nuclear models. However, $\delta\alpha_T$ distributions obtained with the three nuclear models are similar in magnitude and shape, being all flat due to the isotropy of the momentum distribution and the absence of FSIs in our calculations.

We start from a full semi-inclusive model based on the relativistic mean-field theory that produces a five-dimensional cross section which fully describes both lepton and hadron kinematics. To compare with the corresponding one- and two-dimensional experimental cross sections, a change of variables, if necessary, and numerical integrations are subsequently performed. This semi-inclusive framework makes a difference with other approaches implemented in Monte Carlo event generators because it does not rely necessarily on any factorization methods when FSIs are included. Work is in progress to include RMF descriptions in these generators.

To conclude, semi-inclusive neutrino-nucleus reactions where a muon and one proton are detected in the final state can be used, with the right selection of experimental observables, to identify relevant nuclear effects related to both the initial-state dynamics and to final-state interactions, as well as to two-particle/two-hole excitations and thus improve the reconstruction of the neutrino energy. The picture of the interaction drawn by the PWIA is an oversimplification of such complex processes, but it helps very much in providing a clear connection between nuclear modeling and experimentally interesting variables used in the analysis of data. Moreover, it is also a good starting point that highlights the importance of contributions beyond the PWIA necessary for the correct description of the available experimental data. Work is in progress to extend the present analysis using more sophisticated descriptions of the final nucleon dynamics based on the relativistic mean field and also adding 2p2h contributions.

ACKNOWLEDGMENTS

APPENDIX: CONNECTION BETWEEN TKI AND NV

In this Appendix, we deduce Eqs. (23), (24), and (25), which are the single differential cross sections with respect to the transverse kinematic imbalances defined in Eq. (22).

Starting with δp_T, we get

$$\delta p_T^2 = (k'\sin\theta_l + p_N\sin\theta_N^L\cos\phi_N^L)^2 + (p_N\sin\theta_N^L\sin\phi_N^L)^2, \tag{A1}$$

which can be written as a second-degree equation for p_N in the form $ap_N^2 + 2bp_N + c = 0$ with coefficients given by

$$\begin{aligned} a &= \sin^2\theta_N^L, \\ b &= k'\sin\theta_l\sin\theta_N^L\cos\phi_N^L, \\ c &= k'^2\sin^2\theta_l - \delta p_T^2. \end{aligned} \tag{A2}$$

Changing $p_N \to \delta p_T$ and integrating the flux-averaged sixth differential cross section over all the other variables, we obtain the single differential cross section as function of δp_T,

$$\begin{aligned} \frac{d\sigma}{d\delta p_T} = 2\pi &\int_{\theta_l^{\min}}^{\theta_l^{\max}} d\theta_l\sin\theta_l \int_{k'_{\min}}^{k'_{\max}} dk' \int_{\theta_N^{L\,\min}}^{\theta_N^{L\,\max}} d\theta_N^L\sin\theta_N^L \\ &\times \int_{\phi_N^{L\,\min}}^{\phi_N^{L\,\max}} d\phi_N^L \times \langle d^5\sigma\rangle \times \mathcal{J}_p \\ &\times \Theta(p_N - p_N^{\min})\Theta(p_N^{\max} - p_N), \end{aligned} \tag{A3}$$

with $\mathcal{J}_p$ the Jacobian at fixed (θ_N, ϕ_N) expressed as

$$\mathcal{J}_p = \left|\frac{\partial p_N}{\partial(\delta p_T)}\right|_{(\theta_N,\phi_N)} = \left|\frac{\delta p_T}{ap_N + b}\right| \tag{A4}$$

and $\langle d^5\sigma\rangle$ the flux-averaged fifth-differential semi-inclusive cross section. Note that the integrals in Eq. (A3) are performed between general minimum and maximum values. As can be seen in the results section, different kinematic constrains are imposed by the different

neutrino collaborations that need to be taken into account when calculating theoretical predictions to compare with experimental data. Moreover, given a set of variables $(k', \theta_l, \delta p_T, \theta_N^L, \phi_N^L)$, the solution of the second-degree equation for p_N can give no, one, or two valid solutions, understanding a valid solution as a real positive number that fulfills $p_N^{\min} < p_N < p_N^{\max}$. In case of multiple valid solutions, their contributions to the cross section are summed.

Moving to the next variable, $\delta\alpha_T$, we find

$$\cos \delta\alpha_T = \frac{-(k' \sin\theta_l + p_N \sin\theta_N^L \cos\phi_N^L)}{\delta p_T} \quad (A5)$$

with δp_T given in Eq. (A1). Squaring both sides of this equation and solving for θ_N^L, we get

$$\sin \theta_N^L = \frac{k' \sin\theta_l \tan\delta\alpha_T}{p_N(\pm \sin\phi_N^L - \tan\delta\alpha_T \cos\phi_N^L)}, \quad (A6)$$

where $\pm$ arises after taking square root. Therefore, the single differential cross section can be expressed as

$$\frac{d\sigma}{d\delta\alpha_T} = 2\pi \int_{\theta_l^{\min}}^{\theta_l^{\max}} d\theta_l \, \sin\theta_l \int_{k'_{\min}}^{k'_{\max}} dk' \int_{p_N^{\min}}^{p_N^{\max}} dp_N \int_{\phi_N^{L\,\min}}^{\phi_N^{L\,\max}} d\phi_N^L \langle d^5\sigma\rangle \mathcal{J}_\alpha \sin\theta_N^L \Theta(\theta_N^L - \theta_N^{L\,\min})\Theta(\theta_N^{L\,\max} - \theta_N^L) \quad (A7)$$

with $\mathcal{J}_\alpha$ the Jacobian of the change $\theta_N^L \to \delta\alpha_T$ given by

$$\mathcal{J}_\alpha = \left| \frac{\partial\theta_N^L}{\partial\delta\alpha_T} \right| = \left| \frac{(1 + \tan^2\delta\alpha_T)\tan\theta_N^L \sin\phi_N^L}{\tan\delta\alpha_T(\pm \sin\phi_N^L - \tan\delta\alpha_T \cos\phi_N^L)} \right|. \quad (A8)$$

For a fixed set of variables $(k', \theta_l, p_N, \delta\alpha_T, \phi_N^L)$, the value of θ_N^L is calculated following Eq. (A6). To be considered as a valid solution, it must satisfy Eq. (A5) and $\theta_N^{L\,\min} < \theta_N^L < \theta_N^{L\,\max}$.

Finally, $\delta\phi_T$ can easily be linked with ϕ_N^L. Following the definition given in Eq. (22),

$$\delta\phi_T = \phi_N^L - \pi. \quad (A9)$$

Henceforth, the single differential cross section as function of $\delta\phi_T$ is

$$\frac{d\sigma}{d\delta\phi_T} = 2\pi \int_{\theta_l^{\min}}^{\theta_l^{\max}} d\theta_l \, \sin\theta_l \int_{k'_{\min}}^{k'_{\max}} dk' \int_{p_N^{\min}}^{p_N^{\max}} dp_N$$
$$\times \int_{\theta_N^{L\,\min}}^{\theta_N^{L\,\max}} d\theta_N^L \langle d^5\sigma\rangle \sin\theta_N^L. \quad (A10)$$

[1] M. Tanabashi *et al.* (Particle Data Group), Phys. Rev. D **98,** 030001 (2018).

[2] K. Abe *et al.* (T2K Collaboration), Nature (London) **580,** 339 (2020); Nature (London) **583,** E16 (2020).

[3] K. Abe *et al.* (T2K Collaboration), Phys. Rev. D **101,** 112004 (2020).

[4] K. Abe *et al.* (T2K Collaboration), Phys. Rev. D **103,** L011101 (2021).

[5] M. A. Acero *et al.* (NOvA Collaboration), Phys. Rev. Lett. **123,** 151803 (2019).

[6] M. A. Acero *et al.* (NOvA, R. Group), Eur. Phys. J. C **80,** 1119 (2020).

[7] A. A. Aguilar-Arevalo *et al.* (MiniBooNE Collaboration), Phys. Rev. D **81,** 092005 (2010).

[8] A. A. Aguilar-Arevalo *et al.* (MiniBooNE Collaboration), Phys. Rev. D **88,** 032001 (2013).

[9] V. Lyubushkin *et al.* (NOMAD Collaboration), Eur. Phys. J. C **63,** 355 (2009).

[10] G. A. Fiorentini *et al.* (MINERvA collaboration), Phys. Rev. Lett. **111,** 022502 (2013).

[11] L. Fields *et al.* (MINERvA collaboration), Phys. Rev. Lett. **111,** 022501 (2013).

[12] J. Wolcott *et al.* (MINERvA collaboration), Phys. Rev. Lett. **116,** 081802 (2016).

[13] K. Abe *et al.* (T2K Collaboration), Phys. Rev. D **87,** 092003 (2013).

[14] K. Abe *et al.* (T2K Collaboration), Phys. Rev. Lett. **113,** 241803 (2014).

[15] K. Abe *et al.* (T2K Collaboration), Phys. Rev. D **93,** 112012 (2016).

[16] R. Acciarri *et al.* (ArgoNeuT Collaboration), Phys. Rev. D **89,** 112003 (2014).

[17] K. Abe *et al.* (The T2K Collaboration), Phys. Rev. D **98,** 032003 (2018).

[18] X.-G. Lu and others (MINERvA Collaboration), Phys. Rev. Lett. **121,** 022504 (2018).

[19] T. Cai *et al.* (The MINERvA Collaboration), Phys. Rev. D **101,** 092001 (2020).

[20] P. Abratenko *et al.* (MicroBooNE Collaboration), Phys. Rev. D **102,** 112013 (2020).

[21] P. Abratenko *et al.* (MicroBooNE Collaboration), Phys. Rev. Lett. **125**, 201803 (2020).

[22] C. Simpson *et al.* (Super-Kamiokande), Astrophys. J. **885**, 133 (2019).

[23] K. Abe *et al.* (Hyper-Kamiokande Proto-Collaboration), arXiv:1805.04163.

[24] R. Acciarri *et al.* (DUNE Collaboration), arXiv:1512.06148.

[25] J. M. Franco-Patino, J. Gonzalez-Rosa, J. A. Caballero, and M. B. Barbaro, Phys. Rev. C **102**, 064626 (2020).

[26] O. Moreno, T. W. Donnelly, J. W. Van Orden, and W. P. Ford, Phys. Rev. D **90**, 013014 (2014).

[27] J. W. Van Orden and T. W. Donnelly, Phys. Rev. C **100**, 044620 (2019).

[28] P.-O. Löwdin, Phys. Rev. **97**, 1474 (1955).

[29] M. V. Ivanov, A. N. Antonov, J. A. Caballero, G. D. Megias, M. B. Barbaro, E. Moya de Guerra, and J. M. Udias, Phys. Rev. C **89**, 014607 (2014).

[30] X.-G. Lu, L. Pickering, S. Dolan, G. Barr, D. Coplowe, Y. Uchida, D. Wark, M. O. Wascko, A. Weber, and T. Yuan, Phys. Rev. C **94**, 015503 (2016).

[31] L. Pickering, J. Phys. Soc. Jpn. Conf. Proc. **12**, 010032 (2016).

[32] J. M. Franco-Patino, R. Gonzalez-Jimenez *et al.* (to be published).

[33] R. Gonzalez-Jimenez, M. B. Barbaro, J. A. Caballero, T. W. Donnelly, N. Jachowicz, G. D. Megias, K. Niewczas, A. Nikolakopoulos, and J. M. Udias, Phys. Rev. C **101**, 015503 (2020).

[34] G. D. Megias, M. B. Barbaro, J. A. Caballero, J. E. Amaro, T. W. Donnelly, I. R. Simo, and J. W. V. Orden, J. Phys. G **46**, 015104 (2019).

[35] R. González-Jiménez, A. Nikolakopoulos, N. Jachowicz, and J. M. Udías, Phys. Rev. C **100**, 045501 (2019).

[36] G. D. Megias, J. E. Amaro, M. B. Barbaro, J. A. Caballero, T. W. Donnelly, and I. Ruiz Simo, Phys. Rev. D **94**, 093004 (2016).